On the physical interpretation of the lead relation between Warm Water Volume and the El Niño Southern Oscillation

Takeshi Izumo, Matthieu Lengaigne, Jérôme Vialard, Iyyappan Suresh, Yann Planton

On the physical interpretation of the lead relation between Warm Water Volume and the El Niño Southern Oscillation

Takeshi Izumo (1,2), Matthieu Lengaigne (1,2), Jérôme Vialard (1), Iyyappan Suresh (3), and Yann Planton (1)

(1) LOCEAN-IPSL, Sorbonne Université (UPMC, Université Paris 06)- CNRS-IRD-MNHN, Paris, France

(2) Indo-French Cell for Water Sciences, IISc-NIO-IITM-IRD Joint International Laboratory, CSIR-NIO, Goa, India

(3) CSIR-National Institute of Oceanography, Goa, India

Submitted to Climate Dynamics, February 21th, 2018

Revised, June 6th, 2018

Corresponding author: Takeshi Izumo (takeshi.izumo@ird.fr)

Abstract

The warm water volume (WWV), a proxy for the equatorial Pacific heat content, is the most widely used oceanic precursor of the El Niño Southern Oscillation (ENSO). The standard interpretation of this lead relation in the context of the recharge oscillator theory is that anomalous easterlies during, e.g. La Niña, favour a slow recharge of the equatorial band that will later favour a transition to El Niño. Here we demonstrate that WWV only works as the best ENSO predictor during boreal spring, i.e. during ENSO onset, in both observations and CMIP5 models. At longer lead times, the heat content in the western Pacific (WWV_W) is the best ENSO predictor, as initially formulated in the recharge oscillator theory. Using idealised and realistic experiments with a linear continuously stratified ocean model, and a comprehensive wave decomposition method, we demonstrate that spring WWV mostly reflects the fast Kelvin wave response to wind anomalies early in the year, rather than the longer-term influence of winds during the previous year. WWV is hence not an adequate index of the slow recharge invoked in the recharge oscillator. The WWV_W evolution before spring is dominated by forced Rossby waves, with a smaller contribution from the western boundary reflection. WWV_W can be approximated from the integral of equatorial wind stress over the previous ~10 months, thus involving a longer-term time scale than WWV main time scale (~3 months). We hence recommend using WWV_W rather than WWV as an index for the slow recharge before the spring predictability barrier.

Keywords: El Niño Southern Oscillation (ENSO); Warm Water Volume (WWV); ENSO recharge oscillator; equatorial Kelvin and Rossby waves; ENSO precursors; ENSO conceptual models; CMIP5 climate models.

1) Introduction

The El Niño−Southern Oscillation (ENSO) is the leading mode of interannual climate variability on Earth, with tremendous socio-economical and environmental impacts at global scale (e.g. McPhaden et al. 2006; Clarke 2008). Despite significant progress over the past decades in our understanding of the ENSO dynamics, ENSO forecasts still remain a challenge, especially at lead times longer than 10 months (e.g. Barnston et al. 2012). The mechanisms responsible for the growth and termination of El Niño are now reasonably understood. High frequency atmospheric variations, known as Westerly Wind Events, often trigger an El Niño by inducing a Sea Surface Temperature (SST) warming in the central Pacific at the beginning of the year (e.g. Lengaigne et al. 2004a). This initial SST anomaly (SSTA) grows into an El Niño throughout boreal spring and summer due to the Bjerknes feedback (Bjerknes 1969). In this positive ocean-atmosphere feedback loop, positive SSTA induce a wind response (e.g. Gill 1980), whose effect on the ocean induces further warming (e.g. Vialard et al. 2001). This positive feedback is offset by several negative feedbacks, which eventually terminate El Niño events during the following winter. These feedbacks include the instantaneous negative atmospheric feedbacks (e.g. Lloyd et al. 2010; Lengaigne et al. 2006) as well as the delayed negative oceanic feedbacks, at the heart of the oscillatory nature of ENSO.

These delayed negative oceanic feedbacks include (1) a rapid (~6 months) delayed feedback through equatorial Kelvin and first meridional-mode Rossby waves reflections (e.g. Boulanger et al. 2004) and (2) a slower delayed feedback associated with wind-driven equatorial oceanic heat content variations (e.g. Bosc and Delcroix 2008; Zhu et al. 2017). These two oceanic negative feedbacks are encapsulated in the main theoretical frameworks developed to explain the cyclic nature of ENSO. The delayed oscillator (Schopf and Suarez 1988; Battisti and Hirst 1989) and the advective-reflective oscillator (Picaut et al. 1997) both emphasize the role of equatorial wave reflection but stress on different mechanisms. The delayed oscillator highlights the western boundary reflection and the thermocline feedback in the eastern Pacific, while advective-reflective oscillator underscores the eastern boundary reflection and the zonal advection in the central Pacific. While this fast ~6 months oceanic feedback through wave reflections is crucial to understand the equatorial Pacific variability (e.g. Izumo et al. 2016; their Table 1 and Fig. 4), its timescale is much shorter than the observed ENSO spectral peak of 4-5 years. This emphasizes the need of a slower oceanic feedback, which is the focus of another theoretical framework: the recharge oscillator theory, originally introduced by Wyrtki (1985) and later formulated mathematically by Jin (1997a). This slower feedback has been related to the Sverdrup balance (Jin 1997a,b) but also to Rossby wave dynamics (Bosc and Delcroix 2008; Zhang and Clarke 2017; Clarke et al. 2007). In this paradigm, *easterly* wind anomalies during La Niña induce a slow *recharge* in the equatorial Pacific through meridional transport converging in the equatorial band. The thermocline feedback then favours the emergence of positive SSTA, and the development of El Niño, during which westerlies induce an equatorial OHC discharge, thus resulting in a cyclic sequence (Jin 1997a,b).

The original concept of the recharge-discharge theory identified the OHC in the western Pacific as precursor of El Niño, in both Wyrtki (1985) and Jin (1997a) seminal studies. However, the schematic put forward by Jin (1997a) emphasized a recharge throughout the equatorial band. Meinen and McPhaden (2000) further investigated the lead relation between the equatorial Pacific recharge and the ENSO from observations. They introduced the Warm Water Volume (WWV), an index of the total volume of water warmer than 20°C equatorward of 5° in the entire equatorial Pacific, and showed that it was a good ENSO predictor (r~0.6) at lead times of 4-8 months (Fig. 1a). This motivated the inclusion of the WWV (or equivalently the equatorial band OHC) in many analyses, models, or statistical hindcast/forecast schemes of El Niño (e.g. Kessler 2002; Clarke and van Gorder 2003; Ruiz et al. 2005; Dominiak and Terray 2005; Burgers et al. 2005; McPhaden et al. 2006; Drosdowsky 2006; Lima et al. 2009; Kug et al. 2010; Izumo et al. 2010, 2014; Dayan et al. 2014; Yu et al. 2016). The WWV is hence currently monitored in operational centres, which interpret a higher than usual value of WWV as an increased risk for the occurrence of an El Niño. Modelling studies also use early-year WWV as a diagnostic of the oceanic preconditioning for an upcoming El Niño (e.g. Lengaigne et al. 2004b; Fedorov et al. 2014; Hu et al. 2014; Puy et al. 2017). The WWV has thus become a widespread diagnostic of ENSO preconditioning by the oceanic state.

The role of the western Pacific equatorial heat content, rather than that across the entire Pacific, is however emphasized in both seminal (Wyrtki 1985; Jin 1997a,b) and more recent studies (Ramesh and Murtuggude 2013; Boschat et al. 2013; Lai et al. 2015; Ballester et al. 2016; Petrova et al. 2017). There is indeed only a brief time window in spring (roughly from February to April-May) when the WWV is the best predictor of an upcoming El Niño (Fig. 1a). The western Pacific heat content (WWV_W, 120°E-155°W) outperforms the WWV at leads longer than 10 months, as noted by Meinen and McPhaden (2000). After the “spring predictability barrier”, the eastern Pacific heat content (WWV_E, 155°W-80°W) or the typical ENSO indices such as Niño3.4 SSTA become the best predictors of an upcoming El Niño. These two indices – WWV_E and Niño3.4 – are in fact strongly linked because of the strong prevalence of the thermocline feedback in the eastern Pacific (e.g. Vialard et al. 2001; Zelle et al. 2004), and they record the short-term response to wind anomalies in the central Pacific whose influence travel to the eastern Pacific as equatorial Kelvin waves in about two months.

In addition to only being the best predictor over a short time window in early spring, the WWV (WWV_E+WWV_W) also mixes two very different, and opposed, influences (Fig. 1a, WWV_E and WWV_W have a -0.33 correlation). WWV is more correlated with WWV_E (0.74 correlation) than it is with WWV_W (0.40 correlation), suggesting that the WWV is more a metric of the eastern Pacific heat content variations (and hence of the fast response to central Pacific winds) than of the long-term recharge process hypothesized in the recharge oscillator. A role of fast timescales for WWV has also been underlined by the recent studies of McGregor et al. (2016) and Neske and McGregor (2018). The present study hence attempts to further disentangle the exact processes driving ENSO-related equatorial OHC variations and their related indices (WWV_W, WWV_E and WWV). The paper is organized as follows. Section 2 describes the observations, the simulations from the Coupled Model Intercomparison Project Phase 5 (CMIP5; Taylor et al. 2012) and the experiments from a Linear Continuously Stratified (LCS) ocean model used in this paper. Section 3 investigates the physical processes that respectively control WWV_W, WWV_E and WWV by analysing their decomposition into equatorial waves, including the contribution from reflections, and identifying the main wave contributions. This allows obtaining simple wind stress based indices for the observed WWV_W, WWV_E and WWV, hence providing a better understanding of their actual physical meaning and intrinsic timescales. Section 4 summarizes our findings and discusses their implications, notably for ENSO conceptual models and forecasts.

2) Data and models

2.1 Observations, reanalyses and CMIP models data

We use the following observationally-derived products available over the extended historical period (at least from 1871 to 2008): HadiSSTv1 SST (Rayner et al. 2002), Sea Level Anomaly (SLA) from SODA2.2.6 ocean reanalysis (Carton and Giese 2008, Giese and Ray 2011) and surface wind stress from 20CRv2 atmospheric reanalysis (Compo et al. 2011). These long datasets allow to thoroughly assess the statistical significance of the results presented in this study, over the 1900-2008 period (we start from 1900, so as to avoid the less observed 19th century period). We also use the wind stress from ERA-Interim (ERA-I; Dee et al. 2011) atmospheric reanalysis, being one of the best wind products over the recent period (1979-present) in the tropics (Praveen Kumar et al. 2012) and being available in near real-time (20CRv2 being only available until 2008). The ERA-I dataset is used to force the LCS model over the recent period and the OHC interannual variations from this simulation are validated against those derived from the Bureau of Meteorology Research Center (BMRC) tropical Pacific subsurface temperature dataset (based on XBT and TAO/TRITON

Array; Smith 1995), available as monthly WWV time series from 1980 up to present (https://www.pmel.noaa.gov/elnino/upper-ocean-heat-content-and-enso). The above repository provides two types of WWV indices: one based on the 20°C isotherm depth (D20) and the other on 0-300m depth averaged temperature (T300, i.e. OHC). We use the latter one for consistency with the LCS model results based on SLA, although both types of indices are strongly correlated (corr.=0.96 for WWV_W, 0.98 for WWV_E, 0.92 for WWV). T300 indices are multiplied by the surface area of the box over which they are averaged (i.e. in $^oC.m^2$), for consistency with D20-based (in m^3) and SLA-derived (in $cm.m^2$) WWV indices (defined in section 2.3). Results discussed in this paper are robust when D20-based indices are used (not shown), despite a slightly weaker weight to the east Pacific OHC variations (the standard deviation (STD) ratio $STD(WWV_E)/STD(WWV_W) = 1.2$, instead of 1.4 for T300-based indices) arguably because the shallow climatological D20 in the eastern Pacific limits its interannual variability.

We also analyse the monthly SST, wind stress and SLA data from 32 historical simulations in the CMIP5 dataset over the 1861-2005 period (Taylor et al. 2012, see Table S1). When several ensemble members are available, we analyse only the first one in order to give the same weight to each model in the Multi-Model-Mean (MMM). The majority of CMIP5 models exhibits a reasonable ENSO amplitude and spatial SSTA patterns (e.g. Bellenger et al. 2014) as well as a reasonable ENSO seasonal phase locking (e.g. Jourdain et al. 2016), which allows us to use the same index for ENSO peak intensity as in observations, the average November to January (NDJ) SSTA in the Niño3.4 box (170°W-120°W, 5°S-5°N), which captures the main ENSO variability (e.g. Takahashi et al. 2011; we here do not discuss ENSO diversity/continuum, e.g. Capotondi et al. 2015, due to CMIP models difficulty in capturing it, e.g. Graham et al. 2017).

2.2 LCS model

We also use a LCS ocean model (McCreary 1980) to understand the processes driving the WWV variations, using the same configuration as in Izumo et al. (2016). The LCS model allows avoiding the complexity of a general ocean circulation model, without losing the essential physics that drives SLA/OHC variability (contrary to a simpler shallow water model; e.g. Dewitte and Perigaud 1996). It also allows separating explicitly the contribution from the directly forced and the reflected waves on the SLA variations (cf. below). The model domain is the full Indo-Pacific basin, with coastlines defined from the 200-m isobath, including an Indonesian Throughflow (ITF) for the realistic experiments, as in e.g. McCreary et al. (2007). As we will discuss in section 4, the time series of WWV indices in the realistic experiments are however not sensitive to whether the ITF is open or not. Therefore, in the LCS idealised experiment, the ITF is closed for the sake of simplicity.

Background vertical modes are derived from the average stratification over the equatorial Indo-Pacific region (30°E–75°W, 10°N–10°S). These choices result in Kelvin wave speed of 2.5 $m.s^{-1}$ for the 1st baroclinic mode and of 1.5 $m.s^{-1}$ for the 2nd baroclinic mode. The vertical mixing coefficient is set to 4×10^{-8} m^2 s^{-3}, corresponding to a 5-year damping scale for the first baroclinic mode (and a 2-year damping scale for the second baroclinic mode). Results in our paper are quite robust when using 1, 2, 10 and 20-year damping timescales. We retain the first five baroclinic modes but will show that equatorial Pacific OHC interannual variations obtained from the first two modes reproduce most of the observed variations, in agreement with earlier studies (e.g. Chen et al. 1995; Boulanger and Menkes 2001; Shu and Clarke 2002; Izumo et al. 2016; Zhang and Clarke 2017).

We will analyse the physical processes controlling the WWV variations from a LCS simulation forced with 20CRv2 wind stresses over the 1871-2008 period, for the sake of statistical reliability and for efficient filtering of the interdecadal fluctuations. We also performed idealized experiments with ENSO-like westerly wind stress anomalies in the central-western Pacific switched on January 1st of year 0:

$$\tau_x = A\, exp(-((x - x_0)^2/\,\Delta x^2 + y^2/\Delta y^2)/2)$$

with $\Delta x = 25°$, $\Delta y = 7°$, $x_0 = 180°$ and $A = 0.02$ $N.m^{-2}$ (as in Izumo et al. 2016). These parameters have been chosen to match the observed spatial pattern of zonal wind stress regressed on Niño3.4 (not shown).

We analyse our results in the context of the long-wave approximation of the linear theory of equatorial waves (e.g. chapter 11 of Gill 1982). The LCS provides the SLA or current contribution of each baroclinic mode separately. We further separate SLA contributions associated with wave reflections at both boundaries using a dedicated LCS experiment with land points replaced with dampers (e.g. McCreary et al. 1996, Suresh et al. 2016) at both boundaries. In such an experiment, there is no wave reflection as incoming signals are "absorbed" into both boundaries and dissipated. The contribution from wave reflections is obtained as the difference between the control experiment and the damper experiment. See the supplementary information for more details on the procedure to obtain reflected waves and Suppl. Fig. S1 for a validation of the wave decomposition method. Later in the paper, we call "forced" variations the solution that involves no reflections at both boundaries and "reflected" that associated with the residual. We further project those contributions on the waves theoretical meridional SLA structures as in Boulanger and Menkes (1995) for each baroclinic mode in order to obtain the Kelvin and Rossby meridional modes contributions. In the rest of the paper, we will mostly discuss the forced and reflected contributions from the first two baroclinic modes Kelvin (noted K_1 and K_2) and first-meridional mode Rossby (noted $R1_1$ and $R1_2$) waves, which explain the bulk of SLA variations equatorward of 5° (and hence WWV, WWV_E and

WWV_W variations, as we will demonstrate).

2.3 Methods

Our analyses will focus on SLA, which is an accurate proxy for OHC and thermocline depth variations (e.g. Rebert et al. 1985; Gasparin and Roemmich 2016; Palanisamy et al. 2015). SLA, by vertically integrating OHC over the whole water column, is less noisy than the D20, and is observed by satellites allowing a better spatial sampling. We will hence integrate SLA spatially over the western (120°E-155°W), eastern (155°W-80°W) and entire (120°E-80°W) equatorial (5°N-5°S) Pacific as measures of WWV_W, WWV_E, and WWV, respectively. We also use Niño3.4 SSTA and equatorial Pacific zonal wind stress anomalies (hereafter τ_x, averaged over 120°E-80°W; 5°N-5°S, i.e. the WWV region) indices. Long-term trends and decadal-to-multidecadal fluctuations are removed from our 20CRv2 LCS model experiment, SODA reanalysis and CMIP historical simulations using a 14-year window Hanning filter (preserves most of the variance at periods < 7 years; half-power cut at ~10 years). For the analyses of the ERA-I LCS model experiment over the recent 1979-2017 period, we simply detrend the time series through linear regression in order to avoid losing too many endpoints. A 3-month Hanning smoothing is applied for each of these datasets to reduce intraseasonal noise before computing the lag-correlations. Our results are not sensitive to the details of filtering methods (not shown).

Significance tests for regression or correlation coefficients (and correlation critical values) are computed using a Student's two-tailed t-test, assuming one degree of freedom per year (this is justified by the insignificant or negative 1-year lag autocorrelation of the climate indices used in this paper; Bretherton et al. 1999). The consistency between the different CMIP5 models is assessed by showing signals where 70% of models (e.g. Christensen et al. 2013) have the same sign when plotting the MMM. We use a regression approach to diagnose the typical ENSO evolution in the paper, but we have checked using a composite approach that all of our results are to the first order valid for both ENSO phases in observations as well as in CMIP MME, with only some 2nd order assymetries (cf. Suppl. Fig. S2). Therefore, all along this paper, we show by convention results for a "typical" El Niño event (one STD), knowing that they remain the same for a La Niña event, with reversed signs.

2.4 LCS validation

We validate the LCS model forced by ERA-I by comparing the simulated SLA with the observed estimates. Izumo et al. (2016) already demonstrated that this model captures very accurately the equatorial Pacific SLA, thermocline depth and zonal current variability (their Figure

2). Fig. 2 further demonstrates that this simulation also accurately captures the WWV_W, WWV_E and WWV interannual variations, with correlations to observations ranging from 0.86 to 0.92. Our model results exhibit a similar level of agreement with WWV indices computed from the SODA2.2.6 ocean reanalysis, with correlations ranging from 0.84 to 0.90 (not shown). For the extended period, the 20CRv2 LCS simulation also captures the interannual SLA variations simulated by SODA2.2.6 (correlation of 0.78, 0.90 and 0.90 for WWV_W, WWV_E and WWV respectively).

3) Results

3.1 Typical OHC preconditioning and evolution during an El Niño

Fig. 1b provides a lead-correlation analysis of the WWV, WWV_W, WWV_E from SODA reanalysis over the 1900-2008 period with Niño3.4 SSTA in $November_0$-$January_1$ (NDJ_0, the index makes reference to the central month of the period, with 0 designating the year of the ENSO onset and growth and -1 the previous year), i.e. at the ENSO peak. This analysis generally gives very similar results to those derived from observations over the recent 1980-2017 period presented in the introduction (Fig. 1a). Both analyses indicate that Niño3.4 SSTA is a good predictor of ENSO throughout the mature and peak phases thanks to persistence, i.e. roughly from summer to winter. WWV_E exhibits the same behaviour as Niño3.4 SSTA, as expected from the strong coupling between SST and thermocline depth in the central and eastern Pacific (e.g. Zelle et al. 2004). Niño3.4 SSTA and WWV_E lead-correlations however drop before spring (MAM_0), a phenomenon often referred to as the ENSO "spring predictability barrier" (Torrence and Webster 1998). The WWV has higher lead-correlations of ~0.6-0.7 during that spring period. Before that (i.e. at longer leads than 10 months, e.g. in DJF_0, SON_{-1}, and JJA_{-1}), WWV_W outperforms WWV, with a maximum lead-correlation of ~0.4-0.5 around SON_{-1}. These results are broadly consistent with those obtained by Meinen and McPhaden (2000), who did not consider the seasonality and focussed on a shorter period (1980-1999). The WWV index is hence the best ENSO precursor only over a short ~3 months window during spring preceding the ENSO peak.

Figures 1c,d show the same analysis as in Fig. 1a,b but for the long 20CR LCS simulation and CMIP5 MMM respectively. These two datasets reproduce the key features discussed above: WWV_E and WWV_W indices have very different lead-relations with ENSO, the former being the best precursor at short lead time (< 6 months) and the latter being the best predictor at long lead time (> 10 months). WWV is again the best precursor only during a short time window during spring. Individual CMIP5 models generally exhibit a similar behaviour (not shown). The fact that the

WWV variations from the LCS simulation compare very well with observations (Fig. 2) is a strong suggestion that diabatic processes (see e.g. Clarke et al. 2007; Brown and Fedorov 2010; Lengaigne et al. 2012) or the surface heat flux variations (e.g. Forget and Ponte 2015) are second-order processes relative to wind stress-driven WWV variations. And this good agreement suggests that the physical processes controlling these WWV indices are similar in observations, CMIP5 and LCS simulations.

Fig. 3 displays maps of lead-regression of SLA, SSTA and wind stress anomalies onto NDJ_0 Niño3.4 SSTA three to five seasons before the ENSO peak (SON_{-1}, DJF_0 and MAM_0) for SODA. The LCS (not shown) and CMIP5 simulations (Suppl. Fig. S3) give similar results to those of SODA, further asserting that the processes controlling SLA variations are similar in these datasets. As initially suggested by Wyrtki (1985) and Jin (1997a,b), the typical OHC pattern one year before an El Niño (in SON_{-1}, DJF_0) corresponds to a build-up in the western Pacific rather than in the whole equatorial band (Fig. 3a,c). This echoes the analysis of Fig. 1, for which WWV_W is a better ENSO predictor than WWV_E or WWV indices at long leads. This western Pacific build-up exhibits larger loadings off the equator, roughly at the typical latitudes of SLA maxima related to Rossby wave first meridional modes, as expected from linear wave theory, and is associated with easterly wind stress anomalies in the western-central equatorial Pacific and cold SSTA in the eastern Pacific reminiscent of a weak La Niña tendency. This pattern is similar in JJA_{-1} (not shown), but considerably changes in MAM_0, with a positive SLA anomaly along the entire equatorial strip, associated with westerly wind stress anomalies in the western Pacific and positive SSTA along the central-eastern equatorial Pacific (Fig. 3e). This signal is reminiscent of the downwelling Kelvin wave response to westerly wind stress anomalies typical of an El Niño onset, favouring eastward currents and deeper thermocline, and hence SST warming. The strong early-year increase in WWV lead correlation to ENSO on Fig. 3 therefore appears to stem from this Kelvin wave signal. This simple analysis hence suggests that the WWV may be an efficient ENSO precursor in MAM_0 because it captures the downwelling Kelvin wave response, and associated *temporary* recharge, forced by westerly wind anomalies during El Niño onset and development (and related meridional Ekman convergence; e.g. Izumo 2005; McGregor et al. 2016; Zhu et al. 2017; Neske and McGregor 2018). In other words, the WWV in MAM_0 would track the response to zonal wind anomalies (for instance westerly wind events) early in the year, and not only the long-term recharge associated with the recharge oscillator.

The SON_{-1} and DJF_0 SLA patterns not only exhibit a build-up signal in the western Pacific but also negative SLA and SSTA signals in the eastern Pacific (Fig. 3a,c). This zonal seesaw is typical of the rapid thermocline response to equatorial wind stress anomalies, *i.e.* the ENSO zonal tilt mode (e.g. Meinen and McPhaden 2000). This La Niña-type signature one year before the El Niño peak is related to ENSO biennal tendency (e.g. Meehl et al. 2003) as illustrated by the weak negative Niño3.4 correlation at leads longer than 10 months on Fig. 1. This tilt-mode signal could blur a weaker long-term build-up of heat content. To separate those two signals, we estimate the zonal tilt mode associated with the previous year ENSO signal from the lead/lag regression of SLA on Niño3.4 SSTA in SON_{-1}. As this zonal tilt mode and the recharge mode are largely independent (e.g. Jin 1997a,b; Meinen and McPhaden 2000; Alory et al. 2002; Clarke 2010; Thual et al. 2013), we obtain the long-term recharge by regressing out this signal from the total SLA. Fig. 3b,d,f repeats the analysis of Fig. 3a,c,e, but for this "tilt mode independent" SLA pattern. The key features discussed in Fig. 3a,c,e remain robust in this new analysis. The western Pacific OHC (and hence WWV_W) remains the best ENSO predictor at leads longer than one year (also in JJA_{-1}, not shown), irrespective of whether the previous ENSO signal is removed or not. Removing the tilt mode reveals a clear western Pacific wind stress forcing and Kelvin wave response starting in DJF_0 and intensifying in MAM_0. Again, this suggests that the WWV in MAM_0 is influenced by the Kelvin wave response to early-year equatorial Pacific zonal wind stress anomalies, i.e. has a faster timescale than that of the recharge oscillator theory, which involves the influence of previous year's winds. In the following, we will use dedicated LCS experiments to explain the main processes that control the WWV_W, WWV_E and WWV variations.

3.2 Fast recharge and long-term discharge in response to ENSO-like westerly anomalies

In order to illustrate the timescales of the WWV, WWV_E and WWV_W response and explain them in terms of linear equatorial wave theory, we have performed an idealised LCS experiment forced by ENSO-like westerly wind stress anomalies (Fig. 4d, cf. section 2.2). The LCS model starts from rest, with westerly anomalies switched on January 1st of year 0 and maintained constant throughout the simulation. This is a similar problem to that of the basin adjustment to uniform winds described by Philander and Pacanowski (1980), but for an ENSO-like wind anomaly. We will first briefly describe the sea-level response in terms of equatorial waves, before discussing consequences for the WWV, WWV_E and WWV_W indices.

Fig. 4 provides a zonal-time section of equatorial SLA in this experiment (Fig. 4a), along with contributions from the 1st and 2nd baroclinic modes Kelvin and first-meridional Rossby waves, K_1, K_2, $R1_1$ and $R1_2$ (Fig. 4b,c,e,f). These waves dominate the SLA response equatorward of 5°. The first two baroclinic modes indeed dominate the response and the symmetric wind forcing meridional structure projects negligibly on 2nd and higher-order meridional Rossby modes (not shown). At equilibrium, the solution is a balance between the force exerted by the westerly wind stress (Fig. 4d) on the ocean and the pressure gradient associated with the zonal slope of the thermocline (Fig. 4a). The main adjustment is done after one year, and the quasi-equilibrium state is almost reached after three years (Fig. 4a). K_1 and K_2 downwelling waves (Fig. 4b,e) radiate eastward from the wind forcing region, at phase speeds of 2.5 and 1.5 $m.s^{-1}$, reaching the eastern boundary within 1.7 and 2.8 months (propagation times for those starting from the dateline), where they reflect as $R1_1$ and $R1_2$ downwelling waves (Fig. 4c,f), as predicted by the linear equatorial theory. As a result, the sea level is highest in the eastern Pacific within 3-12 months after the forcing is switched on (Fig. 4a). $R1_1$ and $R1_2$ wind-forced upwelling waves radiate westward from the wind forcing region, at a phase speed of -0.8 and -0.5 $m.s^{-1}$, reaching the western boundary within ~3 and ~5 months respectively (Fig. 4c,f), where they reflect as K_1 and a weak K_2 upwelling waves (Fig. 4b,e). As a result, the sea level has its first minimum in the western Pacific within ~6 months of the forcing onset (Figs 4a and 5a).

Fig. 5a shows the temporal evolution of the three WWV indices in this experiment, and Fig. 5b,c display SLA snapshots after 2.5 months (i.e. during the adjustment phase, when WWV is maximum) and 3 years (longer-term adjustment, almost in equilibrium). WWV_W reaches a minimum, close to its quasi-equilibrium value, after about 7 months (Fig. 5a), associated with the $R1_1$ and $R1_2$ wave reflection at the western boundary (Fig. 4b,c,e,f). WWV_E initially increases faster (Fig. 5a), due to the larger propagation speed and stronger projection of Kelvin waves in the 5°N-5°S band (Fig. 5b), but also reaches a maximum after 5-6 months associated with their reflection as slower Rossby waves (Fig. 4b,c,e,f). While WWV_W has reached an almost steady state after 6 months, WWV_E decreases and only stabilizes a couple of years later (Fig. 5a). Fig. 5c shows that this is associated with the asymmetry between reflections at eastern and western boundaries. Coastal Kelvin waves indeed propagate poleward at the eastern boundary, inducing a leakage of positive SLA anomalies toward higher latitudes (Suppl. Figure S4), leading to a weaker positive WWV_E than negative WWV_W at equilibrium (Fig. 5a).

The WWV evolution is the result of two large and opposed contributions from WWV_E and WWV_W (Fig. 5a). The initial WWV response during the first year is a temporary *recharge*, peaking about 2-3 months after the onset of westerly winds (Fig. 5a; due to Ekman convergence, in line with e.g. Izumo 2005; McGregor et al. 2016; Zhu et al. 2017; Neske and McGregor 2018). This recharge results from the strong positive equatorial SLA east of the dateline associated with downwelling Kelvin waves (Fig. 4b) that overcomes the weaker negative SLA to the west associated with the upwelling Rossby waves. This is because (1) the meridional structure of Rossby waves has a relative minimum at the equator, while that of Kelvin waves has a maximum (2) Kelvin waves are at least three times faster than the Rossby waves (3) the typical ENSO wind patch is located slightly west of the basin (Fig. 4d), resulting in Kelvin waves influencing WWV more than Rossby waves (as inferred from additional sensitivity experiments in which wind patch location is changed; not shown). The long-term decrease of WWV_E, associated with leakage toward higher latitudes along the eastern boundary (cf. Suppl. Fig. S4; Wyrtki 1985), however combines with the stable negative WWV_W to yield a long-term *discharge* of WWV under the effect of westerly anomalies, as expected from the recharge oscillator theory.

Overall, the above analyses suggest that the WWV varies as the result of several processes with very different timescales in response to a *westerly* wind: it is first dominated by a fast (2-3 months timescale) *recharge* in response to westerly winds, followed by a longer-term (O(years)) *discharge* caused by a leakage toward higher latitudes at the eastern boundary. This result is robust irrespective of the mixing coefficient or whether the Indonesian Throughflow is closed or not. The fast *recharge* is largely associated with the downwelling Kelvin waves, which have a stronger 5°N-5°S projection than the upwelling Rossby waves. In the real world, where central-west Pacific winds have energetic fluctuations at intraseasonal to interannual timescales, one may thus expect the slow adjustment associated with the long-term discharge to never reach equilibrium, and WWV variations to be dominated by the short-term Kelvin wave response. In the next section, we will perform an in-depth analysis of LCS simulations forced by a realistic wind forcing to show that this is indeed the case in a more realistic context than the idealised experiments analysed above.

3.3 Quantifying the processes controlling WWV indices in a more realistic context

In this section, we analyse the processes controlling WWV_E, WWV_W and WWV in the LCS experiment forced by historical 20CR wind stress described in section 2. We have also verified that the results below are robust in the ERAI-forced experiment. Table 1 quantifies the contributions of the first three baroclinic modes to each WWV index in the 20CR simulation, by providing the regression coefficient of each mode contribution to the total signal (as in Suresh et al. 2013, 2016). Baroclinic modes 1 and 2 explain more than 89% of all three WWV indices variations (95% for WWV), with mode 1 contributing about twice as much as mode 2. Mode 3 contributes marginally (~5-10%), and higher modes can be neglected (not shown). Table 1 further indicates that $K_1 + K_2 + R1_1 + R1_2$ contribute to more than 85% (99% for WWV) of the three WWV indices variability. We will therefore focus on these waves in the following. Since baroclinic modes 1 and 2 have a very similar behaviour (with mode 2 generally lagging mode 1), we will sum their contributions. We will also separate the directly-forced SLA contribution from that involving reflections at both boundaries (cf. section 2). Hereafter, K_f and $R1_f$ (K_r and $R1_r$) designate the sum of the first two baroclinic modes for the forced (reflected) Kelvin and first-meridional mode Rossby waves.

Fig. 6 quantifies the contribution of each of those waves to the equatorial SLA evolution throughout the ENSO cycle, using lead-lag regressions to the observed NDJ_0 Niño3.4 index. Prior to El Niño onset (i.e. before February 0), the equatorial Pacific SLA exhibits a weak La Niña signal, with anomalous easterlies around the dateline (black contours) forcing downwelling to the west of the dateline and upwelling to the east (Fig. 6a). These anomalies switch sign at the El Niño onset (from about March 0 onwards). The zonal westerly wind stresses associated with El Niño are centred near the dateline, and force a downwelling K_f response that propagates to the east and an upwelling $R1_f$ response that propagates to the west (Fig. 6b,d,f). The forced downwelling K_f (upwelling $R1_f$) reflects into a downwelling $R1_r$ (upwelling K_r) at the eastern (western) boundary, as can clearly be seen in Fig. 6d,e (Fig. 6f,g). The reflected waves signals span the entire basin, with diminishing sea level amplitudes from west to east for K_r (Fig. 6g) and from east to west for $R1_r$ (Fig. 6e), as a result of damping along their paths. Those two opposite signals cancel out in the central part of the basin, and the total reflected signal mostly contributes to positive (negative) sea level signals in the eastern (western) Pacific (Fig. 6c). The wave reflection is theoretically about two times more efficient at the eastern than at the western boundary (cf. appendix C of Boulanger and Menkes 1995). I.e. the reflection into Rossby waves is efficient at the eastern boundary, but these waves have a relatively weak projection within 5°N-5°S due to their meridional structure. The Kelvin waves project much more into 5°N-5°S, but their reflection at the western boundary is less efficient. These two factors conspire in yielding SLA signals associated with reflected waves with far smaller amplitudes (Fig. 6c) than those associated with forced waves (Fig. 6b).

Fig. 7 displays the contributions of each of those waves to WWV indices, throughout the ENSO cycle. Due to the smaller amplitude of SLA signals associated with reflected waves (Fig. 6a,b,c), the evolution of all WWV indices is clearly dominated by the forced waves (Fig. 7a,b,c). This is especially striking for WWV, for which the reflected waves almost exactly cancel out (Fig. 7c), due to opposite contributions in the east and west (Fig. 6c). The WWV evolution can thus be largely understood in terms of forced waves (Fig. 7f). The WWV_W evolution is mainly driven by the $R1_f$ response (Fig. 7d). Indeed, there is a 0.93 correlation between WWV_W and $R1_f$ time series (see also Suppl. Fig. S5 for ERAI-forced LCS). While the K_f contribution to WWV_W is on average much weaker ($STD(K_f)/STD(R1_f) = 0.4$), it is not negligible, especially around MAM_0 (Fig. 7d), when ENSO-related westerly anomalies are located in the far west Pacific so that K_f has also a significant contribution on the WWV_W region. The WWV_E evolution is dominated by K_f, with a 0.96 correlation between WWV_E and K_f time series (Suppl. Fig. S5). The $R1_r$ contribution however also contributes ($STD(R1_r)/STD(K_f) = 0.65$), and is almost in phase with K_f (~2 months lag ;Fig. 7e; Suppl. Fig. S5). The opposite K_r contribution is two times weaker than the $R1_r$ one, and $R1_f$ is completely negligible. The sum K_f + $R1_r$ is hence an excellent approximation of WWV_E (0.98 correlation; Suppl. Fig. S5).

As we underlined above, the reflected waves contributions to WWV almost exactly cancel out (Fig. 7c). The WWV variability hence results from a competition between the downwelling K_f signal and the opposite $R1_f$ upwelling signal, which displays a ~3 months lag due to the slower propagation speed of Rossby waves than of Kelvin waves. Regressing K_f+$R1_f$ onto WWV indeed yields WWV≈ 0.78 (K_f + $R1_f$), an approximation that has a 0.83 correlation with the WWV time series (Suppl. Fig. S5). This high correlation confirms that WWV can be generally explained by the sum of the K_f and of the generally-opposite delayed $R1_f$ contributions, with $R1_f$ having a slightly-weaker amplitude (STD(K_f)/STD($R1_f$) = 1.2). The K_f contribution to WWV is larger than that of $R1_f$ (Fig. 7f, Suppl. Fig. S5) due to the stronger projection of the Kelvin wave onto the 5°N-5°S band and to the mean position (within the WWV_W box) of ENSO-related zonal wind interannual variability. As a result, the WWV variations are more correlated to K_f (0.64) than to $R1_f$ (-0.01), indicating that K_f in general tends to dominate WWV variations (STD(K_f)/STD(WWV-K_f) = 1.8, i.e. the K_f amplitude is almost twice larger than the sum of $R1_f$ and the other remaining waves included in the residual WWV-K_f).

The respective contributions of K_f and $R1_f$ signals to the WWV evolution however vary over the ENSO cycle (Fig. 7f). Before the El Niño onset, the K_f upwelling and $R1_f$ downwelling signals cancel each other (with $R1_f$ slightly stronger), resulting in a negligible WWV precursory signal until one year before the peak. During spring (MAM_0), ENSO-related wind stress anomalies (which often occur under the form of Westerly Wind Events, e.g. Lengaigne et al. 2004a) usually appear in the western Pacific (Fig. 6), inducing a fast transition of K_f to a downwelling signal (Fig. 7f). The $R1_f$ signal transitions more slowly from the downwelling signal associated with the previous ENSO phase to an upwelling signal in response to westerlies: it is therefore overall weaker during MAM. As a result, the K_f downwelling signal dominates WWV during MAM_0, with a much weaker contribution of the $R1_f$ downwelling signal (Fig. 7f). From summer onward (JJA_0 and later), as the El Niño grows, the $R1_f$ signal reverses sign to become an upwelling signal, strengthens and damps the K_f downwelling signal. During the El Niño peak and demise, the slower timescale of Rossby waves yields an $R1_f$ upwelling signal that fades more slowly than K_f. $R1_f$ hence explains most of the WWV initial discharge during the El Niño peak phase. Overall, WWV is hence well approximated by K_f + $R1_f$, with a larger amplitude of K_f especially in spring prior to ENSO events, while $R1_f$ tends to become dominant towards the end of ENSO events.

Spring (MAM_0) is the only season when the WWV outperforms the other WWV indices as an ENSO predictor, with WWV_W performing better at longer lead times, and in particular during the previous boreal fall (SON_{-1}). It is hence important to quantify the dominant contributors to WWV in MAM and to WWV_W in SON more precisely, and in particular the relative role of fast timescales (the forced Kelvin wave) and slower ones (the forced Rossby waves, and reflected waves). Fig. 8 illustrates the relative contributions of the fast oceanic response (K_f contribution) and of slower processes (all other waves contributions) to the average WWV in MAM (Fig. 8a) and WWV_W in SON (Fig. 8b) over the 1979-2017 period for the ERA-I forced LCS simulation (we chose ERA-I due to an arguably better wind reconstruction than in 20CR over the recent period, and also to have wind data until 2017, but results are similar with the 20CR-forced experiment; not shown). Contrary to Fig. 7 analysis, Fig. 8 involves no regression to an ENSO index and allows us to directly evaluate the contribution of various waves to the MAM average WWV. This analysis clearly demonstrates that the MAM WWV is indeed dominated by K_f (Fig. 8a). The K_f contribution to MAM WWV has a twice larger STD than that of the other waves and has a 0.84 correlation to WWV, while the sum of all other waves has a 0.15 correlation. This domination by K_f is particularly true for the events with a relatively high WWV in MAM, i.e. prior to all major El Niño events (1982, 1987, 1997 and 2015), and in particular before extreme El Niño events. In MAM prior to the onset of major La Niña events (e.g. 1988, 1998, 2007, 2010), the WWV is generally negative (except in 2010) but the contribution of K_f varies from one event to another: it dominates for some events like in 1988 and 1998, but slower oceanic processes (notably $R1_f$) can also play a strong role in other instances (like in 2007) as expected from delayed negative feedbacks at the end of El Niño events in the delayed oscillator theory (Schopf and Suarez 1988; Battisti and Hirst 1989). The slow oceanic response (mainly $R1_f$, cf. Fig. 7d) dominates the SON WWV_W variability, with a much weaker K_f contribution (~3 times weaker STD) in any ENSO phase (Fig. 8b). Overall, this section hence demonstrates the strong predominance of the fast forced Kelvin wave in the MAM WWV variations, while the SON WWV_W is dominated by slower timescales (and in particular $R1_f$).

3.4 Explaining WWV_W, WWV_E and WWV through simple wind stress-based proxies

The contributions from the K and R1 forced and reflected waves can in principle be estimated from wind stress variations during the preceding months. On the basis of the section 3.3 results, we will now examine whether WWV indices can be approximated by simple proxies based on equatorial wind stress anomalies.

The above analysis suggests that WWV_W is mainly driven by $R1_f$. The typical timescale for R1 to cross the basin is ~8 months for the 1st and ~14 months for the 2nd baroclinic mode. WWV_W should thus be related to the time integral of the equatorial Pacific (5°N-5°S, 120°E-80°W) zonal wind stress anomaly τ_x over the previous ~10 months:

$$\tau_{10}(t) = \int_{-10\,months}^{0} \tau_x(t - t')dt' \qquad (1)$$

i.e. τ_{10} represents the integral of τ_x anomaly along the equatorial Pacific over the last 10 months. Integrating the zonal wind stress over the entire equatorial strip rather than a box more focussed on the usual forcing region in the central-west Pacific allows us also to integrate the effect of early-year wind anomalies (that are shifted westward) or opposite anomalies in the east during the ENSO peak. Fig. 9a shows that $-\tau_{10}$ (red curve) does a reasonable job in explaining the typical observed WWV_W phase relationship with ENSO (WWV_W has a 0.82 correlation with $-\tau_{10}$ in our 20CR-forced historical LCS experiment over ~100 years; the minus sign comes from the fact that westerlies force upwelling Rossby waves). Note that similar correlations – in the 90% confidence limit – are obtained when integrating over the last ~5-14 months, i.e. the 10 months timescale is indicative. Similar results can be obtained from CMIP5 models (cf. Suppl. Fig. S6). Fig. 10a further illustrates that the time evolution of this WWV_W wind proxy is able to accurately explain most of the recent observed WWV_W interannual variations over the last ~35 years (corr. = 0.75).

The WWV_E evolution is dominated by K_f, with non-negligible, almost-in-phase (~2 months lag) $R1_r$ contribution (cf. section 3.3). The typical timescale for Kelvin wave signals to cross the basin is about 3 months (e.g. Fig. 6g). This matches qualitatively with the timescales estimated from theoretical wave speeds (2.7 months for the first baroclinic mode Kelvin wave). WWV_E should thus be related to the integral of the basin-averaged 5°N-5°S zonal wind stress anomalies roughly over the previous ~3 months, noted τ_3. Fig. 9b confirms that τ_3 matches well the typical observed WWV_E phase relationship with ENSO. And WWV_E indeed has a 0.87 correlation to τ_3 in our 20CR-forced historical LCS experiment over ~100 years (here the positive sign results from the fact that the westerlies force downwelling Kelvin waves; note that similar correlations – in the 90% confidence limit – are obtained when integrating over the last ~1-6 months). As shown on Suppl. Fig. S6, this is also the case for CMIP5 models, except for ENSO decay phase (possibly due to CMIP typical biases, e.g. Brown et al. 2014). Fig. 10b also illustrates that the time evolution of τ_3 accurately captures most of the observed WWV_E interannual variations (corr.=0.9).

Finally, we have shown that the WWV evolution is dominated by the balance between the forced Kelvin and Rossby waves. As for WWV_E, the K_f contribution to WWV can be roughly approximated by τ_3 ($K_{f\_WWV} \approx 6.4 \pm 0.6 \times 10^{15}\, \tau_3$; corr.= 0.88). The opposite and delayed $R1_f$ contribution to WWV can be approximated by $-\tau_{10}$ ($R1_{f\_WWV} \approx -6.1 \pm 0.7 \times 10^{15}\, \tau_{10}$; corr.= 0.81). We hence can simply sum these two forcing terms to obtain the following proxy for WWV:

$$WWV \approx C\,(\tau_3 - \tau_{10}) \qquad (2)$$

a proxy that has a 0.64 correlation with the actual LCS WWV time series (C being a constant obtained from regression, C = 4.8 x 10^{15} $cm.m^4.N^{-1}$, for WWV in $cm.m^2$, and τ_3 and τ_{10} in $N.m^{-2}$). This confirms that the WWV can be reasonably well explained by a combination of τ_3 and the opposite delayed τ_{10} contribution, with the latter having a slightly-weaker amplitude (STD ratio of 0.8). Note however that, as for the equation $WWV \approx K_f + R1_f$ (cf. section 3.3), the total WWV variability is more correlated to the first term (corr. =0.44) than to the second one (corr. =-0.01). This WWV wind forcing proxy is able to accurately capture the typical WWV evolution during ENSO events in observations (Fig. 9c) and CMIP5 models (Suppl. Fig. S6). Fig. 10c further demonstrates that equation (2) explains most of the observed WWV interannual variations since 1980 (corr.=0.76).

Overall, we have shown in this section that the three WWV indices can be reasonably approximated through simple wind stress based proxies of the various wave contributions to sea level. WWV_E is dominated by the influence of the forced Kelvin wave and almost-in-phase reflected $R1_r$ wave. WWV_W is dominated by the opposite influence of the forced Rossby wave with a weaker contribution from the forced Kelvin wave. WWV combines K_f and $R1_f$, with the Kelvin wave contribution dominating, notably in spring, at the beginning of ENSO events, explaining why the WWV then becomes the best ENSO predictor.

4) Summary and Discussion

4.1 Summary

ENSO predictability is grounded on the ocean memory: the warm water volume (WWV), a proxy for the equatorial Pacific heat content, is a widely used predictor of ENSO. This lead relation between WWV and ENSO is usually interpreted in the context of the recharge oscillator theory as a long-term response of the equatorial heat content to wind variations during the previous years. In the present study, we have used observations, CMIP5 historical simulations, and idealized and realistic LCS experiments with a proper equatorial wave decomposition to challenge that interpretation. Idealized experiments first illustrate that the response to switched-on ENSO-like westerlies involves a fast (~3 months timescale) WWV recharge, associated with the imprint of equatorial Kelvin waves in the 5°N-5°S band. A WWV discharge only overcomes this initial recharge after 2-3 years, and is largely due to coastal Kelvin waves carrying the positive sea level anomalies poleward in the eastern Pacific, as initially suggested by Wyrtki (1985; rather than to the Sverdrup transport discharge effect suggested by Jin 1997a,b). Since there are energetic variations of wind stress in the central Pacific at intraseasonal to interannual timescales, this simple experiment suggests that equatorial Kelvin waves may dominate the short-term WWV variations.

We then demonstrate that the WWV variations in experiments forced by realistic wind stresses are dominated by forced waves, due to the almost exact cancellation of reflected waves contributions. Since first-baroclinic mode first-meridional mode Rossby waves typically take 10 months to cross the basin, this provides an upper limit to the WWV adjustment timescale. We further show from observations, LCS experiments and CMIP5 models that WWV serves as the best predictor of the upcoming ENSO event only in spring (MAM_0): WWV_W performs better at longer lags, and WWV_E or Niño3.4 SST perform better at shorter lags. In MAM_0, WWV variations are dominated by the downwelling Kelvin wave contribution in response to wind anomalies during the preceding 3 months (i.e. the forced Rossby wave contribution to WWV is relatively weak in MAM_0). More specifically, the WWV at this time does not generally reflect the influence of the previous phase of the ENSO cycle, as opposed to what was suggested by the summarizing sketches in Jin (1997a,b) and Meinen and McPhaden (2000).

The best ENSO predictor at 10 to 18 months lead times (i.e. before ENSO spring predictability barrier) is the WWV_W. At these lead times, the WWV_W build-up is dominated by the first and second baroclinic modes first meridional mode Rossby wave $R1_f$. This is further confirmed by the good match between the WWV_W and the integral of equatorial Pacific-averaged zonal wind stress anomalies over the last 10 months τ_{10} (e.g. 0.75 correlation in observations, cf. Fig. 10a). WWV_W hence contains information about wind anomalies during the previous ENSO phase.

Based on the above results, we suggest, as initially put forward in Wyrtki (1985) and in Jin (1997a,b) analytical development, that the WWV_W is a better index of the long-term ocean memory from the *previous* ENSO phase than WWV, which largely reflects the shorter-term (~3 months timescale) equatorial Kelvin wave response to wind anomalies during the early stage of an *upcoming* ENSO event.

4.2 Discussion

The spring WWV is used as an index of the long-term memory of ENSO in the framework of the recharge oscillator theory in many studies (e.g. Meinen and McPhaden 2000; Kessler 2002; Clarke and Van Gorder 2003; Lengaigne et al. 2004; McPhaden et al. 2006; Fedorov et al. 2014; Hu et al. 2014; McGregor et al. 2016; Puy et al. 2017; Neske and McGregor 2018). Our results indicate that spring WWV is not a relevant index to describe the slow equatorial heat content build-up that results from *easterly* anomalies and leads to a phase transition in the recharge oscillator theory. We indeed show that WWV in boreal spring is mainly influenced by forced Kelvin waves, which have a timescale of ~3 months, in agreement with McGregor et al. (2016), Zhu et al. (2017) and Neske and McGregor (2018) who found that equatorial or off-equatorial westerly wind stress anomalies can induce a rapid WWV recharge through Ekman convergence during ENSO onset. All of these studies however still interpret the WWV as an index of the long-term memory of ENSO in the framework of the recharge oscillator paradigm, despite the temporary nature of this recharge. Those results however imply that spring WWV contains more information from wind variations during the last few months than during the previous year, i.e. during the previous ENSO phase. Our study does not imply that the recharge oscillator theory is incorrect. While reflected waves do not contribute to WWV because they cancel out, they indeed have significant impacts on thermocline variations near both boundaries and zonal currents throughout the basin (cf. Suppl. Fig. S7), and hence can affect SST (and the Bjerknes feedback) through the thermocline and zonal advective feedbacks (e.g. Picaut et al. 1997; Vialard et al. 2001; Izumo et al. 2016 among others). Our study rather implies that spring WWV is not a good measure of the slow recharge of this theory, with fall WWV_W being a better measure of it. The fact that WWV is not an appropriate measure of the long-term recharge invoked in the recharge oscillator could for instance explain why recent studies have questioned the relevance of the recharge oscillator on the basis of the analysis of WWV variations (Linz et al. 2014; Graham et al. 2015; Lu et al. 2017).

The comprehensive quantification of the different wave contributions to the WWV evolution in the present study demonstrates that the WWV is dominated by its short-term component. A recent study (Neske and McGregor 2018) quantified the contribution from the instantaneous wind response to the WWV evolution and found that roughly half of the WWV variations arise from wind forcing in the past three months. While the two studies agree qualitatively, our study suggests a larger contribution of fast timescales. This may arise from several causes. First, we use a different methodology from Neske and McGregor (2018) to isolate fast timescales. Neske and McGregor (2018) do not separate contributions from the Kelvin/Rossby and forced/reflected waves as in the present study, and rather define the instantaneous contribution as the signal induced by the wind over the last three months. This "instantaneous" response mixes K_f and $R1_f$ as well as a part of the reflected waves (Kelvin waves can cross the basin in less than 3 months). Second, there is a significant contribution from the 2nd baroclinic mode to WWV variability in our study, that is neglected by the Neske and McGregor (2018) shallow water model. Many past studies (e.g. Chen et al. 1995; Boulanger and Menkes 2001; Shu and Clarke 2002; Izumo et al. 2016; Zhang and Clarke 2017) have shown the importance of the second baroclinic mode for ENSO-related equatorial thermocline depth variations. Including the 2nd baroclinic mode in our model increases the dominance of K_f, since $K_{f,2}$ is fast enough to be rather in-phase with $K_{f,1}$ and amplifies it, while the slower $R1_{f,2}$ does not, being less in phase with $R1_{f,1}$ (not shown). Due to those methodological differences, it is not straightforward to compare our results with Neske and McGregor (2018) quantitatively, but they both qualitatively indicate that at least half of the WWV variance has a fast timescale.

In agreement with some previous studies (Wyrtki 1985; Ramesh and Murtuggude 2013; Lai et al. 2015; Graham et al. 2015; Ballester et al. 2015, 2016), our results indicate that the slow preconditioning rather occurs in the western Pacific. We also demonstrate that the WWV_W evolution can be largely explained by the wind stress forcing over the preceding ~10 months (this integration period can be varied over the last 5 to 14 months with a statistically indistinguishable skill). This result may however appear to be a bit inconsistent with the analytical results of Fedorov (2010), which indicated that the WWV_W can be approximated by the temporal integral of the zonal wind stress forcing over a longer period (plus a weaker faster tilt mode contribution). Our 10 months timescale is indeed shorter than the observed ENSO half-period (~4-5 years/2), suggesting that the WWV_W index may not fully capture ENSO long-term recharge processes. The fast oceanic adjustment over the equatorial band may explain why the current WWV_W index is largely explained by the wind variations over the preceding 10 months. Fig. 3 however shows that the OHC preconditioning in fall before ENSO onset not only occurs over the western equatorial Pacific but also over the southwest Pacific, a region not encompassed in the current WWV_W index. The influence of this region on ENSO evolution has already been suggested in previous studies (e.g. Alory and Delcroix 2002; Cibot et al. 2005; and in Wen et al. 2014, but only in spring). Preliminary analyses suggest that a WWV_W extended to the southern Pacific, where off-equatorial Rossby waves propagation are slower, may indeed be a better index (notably in previous fall before ENSO onset) to fully integrate the wind information and capture the slower long-term recharge related to the recharge oscillator theory.

Our results are robust when we use different choices for analysing the LCS model results. Our results are unaffected irrespectively of whether we use an open/closed throughflow to the Indian Ocean (and the variations of the WWV indices are equally realistic in both cases), of the dissipation timescale used in the model, when using different wind forcing products (see e.g. Suppl. Fig. S7, equivalent of Fig. 6 for ERAI-forced LCS), or when analysing the results over a different period.

Our results demonstrate that WWV_W is the best oceanic predictor of ENSO at long-lead (>10 months) in all the datasets we analysed (observations, ocean reanalyses, LCS experiments forced by different wind products, CMIP simulations). The physical mechanisms by which WWV_W can favour an ENSO onset/phase transition is however still unclear. The original recharge theory suggested that a recharged state would favour positive thermocline depth anomalies and warmer

SST through the thermocline feedback. The thermocline variability in the western Pacific indeed weakly influences SST there, due to the thermocline being very deep in that region. The thermocline feedback however mostly operates in the eastern Pacific where the thermocline is shallow (e.g. Vialard et al. 2001), whereas SST is the closest to the deep atmospheric convection threshold (e.g. Graham and Barnett 1987), and hence favourable to induce an atmospheric response, in the western-central Pacific. Therefore, identifying the mechanism that acts to link a recharged WWV_W with SSTA in the central Pacific is the next challenge. Some studies have suggested that heat content variations could influence central Pacific SST through zonal current anomalies (e.g. Jin and An 1999; Zhang et al. 2007). Recent studies have also suggested that the subsurface zonal advection of western Pacific heat content anomalies by the equatorial undercurrent could also play a role (Ballester et al, 2016). There is hence yet no consensus on the precise mechanisms through which a recharge/discharge in the western Pacific at the end of the year could influence central Pacific SSTA during the following spring. We hope that the present study will provide some guidance for future studies attempting to ground the lead relation of equatorial Pacific heat content anomalies to ENSO with physical explanations that are compatible with observations.

Acknowledgments Takeshi Izumo, Matthieu Lengaigne, and Jérome Vialard, funded by IRD, gratefully acknowledge the CSIR-National Institute of Oceanography (NIO, Goa, India) for hosting them during their stays there, and would like to thank their colleagues at NIO for their hospitality and help. This work was mainly done while TI and ML were visiting scientists at the NIO, under Institut de Recherche pour le Développement (IRD) funding. Yann Planton was funded by the Belmont project GOTHAM, under grant ANR-15-JCLI-0004-01. This is NIO contribution 6244. The NOAA FERRET software was used here for analysis.

References

Alory, G, Delcroix T (2002) Interannual sea level changes and associated mass transports in the tropical Pacific from TOPEX/Poseidon data and linear model results (1964–1999). J Geophys Res Ocean 107(C10). doi:10.1029/2001JC001067

Ballester, J,, Bordoni S, Petrova D, Rodó X (2015) On the dynamical mechanisms explaining the western Pacific subsurface temperature buildup leading to ENSO events. Geophys Res Lett 42: 2961–2967. doi:10.1002/2015GL063701.

Ballester, J. et al. (2016) Sensitivity of El Niño intensity and timing to preceding subsurface heat magnitude. Sci Rep 6:36344; doi: 10.1038/srep36344

Barnston AG, Tippett MK, L'Heureux ML, Li S, DeWitt DG (2012) Skill of real-time seasonal ENSO model predictions during 2002–11: is our capability increasing? Bull Am Meteorol Soc 93(5):631–651. doi:10.1175/BAMS-D-11-00111.1

Battisti DS, Hirst AC (1989) Interannual variability in the tropical atmosphere-ocean model: influence of the basic state, ocean geometry and nonlineary. J Atmos Sci 45:1687–1712

Bellenger, H, Guilyardi E, Leloup J, Lengaigne M,, Vialard J (2014) ENSO representation in climate models: from CMIP3 to CMIP5. Clim Dyn 42:1999-2018. doi:10.1007/s00382-013-1783-z

Bjerknes J (1969) Atmospheric teleconnections from the equatorial Pacific. Mon Weather Rev 97:163–172

Bosc C, Delcroix T. (2008) Observed equatorial Rossby waves and ENSO ‐ related warm water volume changes in the equatorial Pacific Ocean. J Geophys Res Ocean 113(C6). doi:10.1029/2007JC004613

Boschat G, Terray P, Masson S (2013) Extratropical forcing of ENSO. Geophys Res Lett *40*(8): 1605-1611. doi: 10.1002/grl.50229

Boulanger J-P, Menkes C (1995) Propagation and reflection of long equatorial waves in the Pacific Ocean during the 1992–1993 El Niño. J Geophys Res Ocean 100(C12): 25041-25059. doi:10.1029/95JC02956

Boulanger J-P, Menkes C (2001) The TRIDENT Pacific model: II. The thermodynamical model and the role of long equatorial wave reflection during the 1993–1998 TOPEX/POSEIDON period. Clim Dyn 17:175–186. doi:10.1007/PL00013734

Boulanger J-P, Menkes C, Lengaigne M (2004) Role of high- and low- frequency winds and wave reflection in the onset, growth and termination of the 1997–1998 El Niño. Clim Dyn 22(2–3):267–280. doi:10.1007/s00382-003-0383-8

Bretherton CS, Widmann M, Dymnikov VP, Wallace JM, Bladé I (1999) The effective number of spatial degrees of freedom of a time-varying field. J Clim *12*(7):1990-2009.

Brown JN, Fedorov AV (2010) Estimating the diapycnal transport contribution to warm water volume variations in the tropical Pacific Ocean. J Clim 23:221–237. doi:10.1175/2009JCLI2347.1

Brown JN, Langlais C, Maes, C (2014) Zonal structure and variability of the Western Pacific dynamic warm pool edge in CMIP5. Clim Dyn 42:3061–3076. doi:10.1007/s00382-013-1931-5

Burgers G et al. (2005) The simplest ENSO recharge oscillator. Geophys Res Lett 32(13):L13706.

doi:10.1029/2005GL022951

Capotondi A, Wittenberg AT, Newman M et al. (2015) Understanding ENSO diversity. Bull Am Meteorol Soc 96(6):921-938. doi:10.1175/BAMS-D-13-00117.1

Carton JA and Giese BS (2008) A reanalysis of ocean climate using Simple Ocean Data Assimilation (SODA). *Monthly Weather Review*, *136*(8), 2999-3017.

Chen D, Zebiak SE, Busalacchi AJ,, Cane MA (1995) An improved procedure for EI Nino forecasting: implications for predictability. Science *269*(5231):1699-1702. doi:10.1126/science.269.5231.1699

Christensen JH, Krishna Kumar K, Aldrian E, et al. (2013) Climate phenomena and their relevance for future regional climate change. In T. F. Stocker, et al. (Eds.), Climate Change 2013: The Physical Science Basis. Contribution of Working Group I to the Fifth Assessment Report of the Intergovernmental Panel on Climate Change (pp. 1217–1308). Cambridge, UK, and New York: Cambridge University Press.

Cibot C, Maisonnave E, Terray L, .Dewitte B (2005) Mechanisms of tropical Pacific interannual-to-decadal variability in the ARPEGE/ORCA global coupled model. Clim Dyn 24: 823. doi:10.1007/s00382-004-0513-y

Clarke AJ, Van Gorder S (2003) Improving El Niño prediction using a space-time integration of Indo-Pacific winds and equatorial Pacific upper ocean heat content. Geophys Res Lett 30(7):1399. doi:10.1029/2002GL016673

Clarke AJ,.Van Gorder S, Colantuono G (2007) Wind stress curl and ENSO discharge/recharge in the equatorial Pacific. J Phys Oceanogr 37:1077–1091. doi:10.1175/JPO3035.1

Clarke AJ (2008) An introduction to the dynamics of El Niño & the Southern Oscillation. Elsevier (Academic Press). ISBN: 978-0- 12-088548-0

Clarke AJ (2010) Analytical theory for the quasi-steady and low-frequency equatorial ocean response to wind forcing: The tilt and warm water volume modes. J. Phys. Oceanogr 40(1): 121–137. doi:10.1175/2009JPO4263.1.

Compo GP, Whitaker JS, Sardeshmukh PD, Matsui N, Allan RJ, Yin X, Worley SJ (2011) The twentieth century reanalysis project. QJ R Meteorol Soc 137(654):1–28. doi:10.1002/qj.776

Dayan H, Vialard J, Izumo T, Lengaigne M (2014) Does sea surface temperature outside the tropical Pacific contribute to enhanced ENSO predictability? Clim Dyn. doi:10.1007/s00382-013-1946-y

Dee DP et al (2011) The ERA-Interim reanalysis: configuration and performance of the data assimilation system. Q J R Meteorol Soc 137:553–597. doi:10.1002/qj.828

Dewitte B, Perigaud C (1996). El Niño-La Niña events simulated with Cane and Zebiak's model and observed with satellite or in situ data. Part II: Model forced with observations. J Clim 9(6): 1188-1207

Dominiak S, Terray P (2005) Improvement of ENSO prediction using a linear regression model with a southern Indian Ocean sea surface temperature predictor. Geophys Res Lett *32*(18). doi:10.1029/2005GL023153

Drosdowsky W (2006) Statistical prediction of ENSO (Niño 3) using sub-surface temperature data. Geophys Res Lett *33*(3). doi:10.1029/2005GL024866

Fedorov AV (2010) Ocean response to wind variations, warm water volume, and simple models of ENSO in the low-frequency approximation. J Clim 23:3855–3873.doi:10.1175/2010jcli3044.1

Fedorov AV, Hu S, Lengaigne M, Guilyardi E (2014) The impact of westerly wind bursts and ocean initial state on the development, and diversity of El Niño events. Clim Dyn. doi:10.1007/s00382-014-2126-4

Forget G, Ponte RM (2015) The partition of regional sea level variability, Prog Oceanogr 137:173–195. doi:10.1016/j.pocean.2015.06.002

Gasparin F, Roemmich D (2017) The seasonal march of the equatorial Pacific upper-ocean and its El Niño variability. Prog Oceanogr *156*:1-16. doi:10.1016/j.pocean.2017.05.010

Giese BS, Ray S (2011) El Niño variability in simple ocean data assimilation (SODA), 1871–2008. J Geophys Res 116(C2):C02024. doi:10.1029/2010JC006695

Gill AE (1980) Some simple solutions for heat-induced tropical circulation. Q J R Meteorol Soc 106:447–462. doi:10.1002/qj.49710644905

Gill AE (1982) *Atmosphere-Ocean dynamics (International Geophysics Series)*. academic press.

Graham NE, Barnett TP (1987) Sea surface temperature, surface wind divergence, and convection over tropical oceans. Science *238*(4827):657-659. doi:10.1126/science.238.4827.657

Graham FS, Brown JN, Wittenberg AT, Holbrook NJ (2015) Reassessing conceptual models of ENSO. J Clim 28:9121–9142. doi:10.1175/JCLI-D-14-00812.1

Graham FS, Wittenberg AT, Brown JN. Marsland SJ, Holbrook NJ (2017) Understanding the double peaked El Niño in coupled GCMs. Clim Dyn *48*(5-6):2045-2063.

Hu S, Fedorov AV, Lengaigne M, and Guilyardi E (2014) The impact of westerly wind bursts on the diversity and predictability of El Niño events: An ocean energetics perspective. Geophys Res Lett 41:4654–4663, doi:10.1002/2014GL059573

Izumo T (2005) The equatorial undercurrent, meridional overturning circulation, and their roles in mass and heat exchanges during El Niño events in the tropical Pacific Ocean. Ocean Dyn *55*(2):110-123. doi:10.1007/s10236-005-0115-1

Izumo T, Vialard J, Lengaigne M, de Boyer Montegut C, Behera SK, Luo JJ, Cravatte S, Masson S, Yamagata T (2010) Influence of the state of the Indian Ocean Dipole on the following year's El Niño. Nat Geosci 3:168–172. doi:10.1038/ngeo760

Izumo T, Lengaigne M, Vialard J, Luo J-J, Yamagata T, Madec G (2014) Influence of Indian Ocean Dipole and Pacific recharge on following year's El Niño: interdecadal robustness. Clim Dyn 42(1–2):291–310. doi:10.1007/s00382-012-1628-1

Izumo T, J. Vialard, H. Dayan, M. Lengaigne, I. Suresh (2016) A simple estimation of equatorial Pacific response from windstress to untangle Indian Ocean Dipole and Basin influences on El Niño. Clim. Dyn. 46 (7), 2247-2268. doi:10.1007/s00382-015-2700-4

Jin FF (1997a) An equatorial ocean recharge paradigm for ENSO. Part I: conceptual model. J Atmos Sci 54:811–829

Jin FF (1997b) An equatorial ocean recharge paradigm for ENSO. Part II: a stripped-down coupled model. J Atmos Sci 54:830–847

Jin FF, An SI (1999) Thermocline and zonal advective feedbacks within the equatorial ocean recharge oscillator model for ENSO. Geophys Res Lett 26:2989–2992. doi:10.1029/1999GL002297.

Jourdain NC, Lengaigne M, Vialard J, Izumo T, Gupta AS (2016) Further insights on the influence of the Indian Ocean dipole on the following year's ENSO from observations and CMIP5 models. J Clim 29(2):637-658. doi:10.1175/JCLI-D-15-0481.1

Kessler WS (2002) Is ENSO a cycle or a series of events? Geophys Res Lett 29(23):2125. doi:10.1029/2002GL015924

Kug, JS, Sooraj KP, Li T, Jin FF (2010) Precursors of the El Niño/La Niña onset and their interrelationship**.** J Geophys Res 115(D5). doi:10.1029/2009JD012861

Praveen Kumar B, Vialard J, Lengaigne M, Murty VSN, Mcphaden MJ, Cronin MF, Pinsard F, Reddy KG (2013) TropFlux wind stresses over the tropical oceans: evaluation and comparison with other products. Clim Dyn *40*(7-8):2049-2071. doi: 10.1007/s00382-012-1455-4

Lai AWC, Herzog M, Graf HF (2015) Two key parameters for the El Niño continuum: zonal wind anomalies and Western Pacific subsurface potential temperature. Clim Dyn 45(11-12):3461-3480. doi:10.1007/s00382-015-2550-0

Lengaigne M, Boulanger JP, Menkes C, Delecluse P, Slingo J (2004a) Westerly Wind Events in the tropical Pacific and their influence on the coupled ocean–atmosphere system: a review. Earth's Clim Ocean atmos Interact:49–69. doi:10.1029/147GM03

Lengaigne M, Guilyardi E, Boulanger JP, Menkes C, Delecluse P, Inness P, Cole J, Slingo J (2004b) Triggering of El Niño by Westerly Wind Events in a coupled general circulation model. Clim Dyn 23(6):601–620. doi:10.1007/s00382-004-0457-2

Lengaigne M, Hausmann U, Madec G, Menkès C, Vialard J, and Molines JM (2012) Mechanisms controlling warm water volume interannual variations in the equatorial Pacific: diabatic versus adiabatic processes. Clim Dyn *38*(5-6):1031-1046. doi :10.1007/s00382-011-1051-z

Lengaigne M, Boulanger J-P, Menkes C, Spencer H (2006) Influence of the seasonal cycle on the termination of El Niño events in a coupled general circulation model. J Clim 19(9):1850–1868. doi:10.1175/JCLI3706.1

Lengaigne M, Hausmann U, Madec G, Menkès C, Vialard J, and Molines JM (2012) Mechanisms controlling warm water volume interannual variations in the equatorial Pacific: diabatic versus adiabatic processes. Clim Dyn *38*(5-6):1031-1046. doi :10.1007/s00382-011-1051-z

Lima CH, Lall, U, Jebara T, Barnston, AG (2009) Statistical prediction of ENSO from subsurface sea temperature using a nonlinear dimensionality reduction. J Clim *22*(17):4501-4519. doi:10.1175/2009JCLI2524.1

Linz M, Tziperman E, and MacMartin DG (2014) Process-based analysis of climate model ENSO simulations: Intermodel consistency and compensating errors, J Geophys Res *119*:7396–7409, doi:10.1002/2013JD021415

Lloyd J, Guilyardi E, Weller H (2010) The role of atmosphere feedbacks during ENSO in the CMIP3 models. Part II: using AMIP runs to understand the heat flux feedback mechanisms. Clim Dyn 37:1271–1292. doi:10.1007/s00382-010-0895-y

Lu Q, Ruan Z, Wang DP, Chen D, Wu Q (2017) Zonal Transport from the Western Boundary and Its Role in Warm Water Volume Changes during ENSO. J Phys Oceanogr 47(1):211-225. doi:10.1175/JPO-D-16-0112.1

McCreary JP (1980) Modelling wind-driven ocean circulation. JIMAR 80-0029, HIG 80-3, Univ. of Hawaii, Honolulu, p. 64

McCreary JP, Han W, Shankar D, Shetye SR (1996) Dynamics of the East India Coastal Current: 2. Numerical solutions. J Geophys Res *101*(C6):13993-14010. doi:10.1029/96JC00560

McCreary JP, Miyama T, Furue R, Jensen T, Kang H-W, Bang B, Qu T (2007) Interactions between the Indonesian Throughflow and circulations in the Indian and Pacific Oceans. Prog Oceanogr 75(1):70–114. doi:10.1016/j.pocean.2007.05.004

McGregor S, Timmermann A, Jin FF, Kessler WS (2016) Charging El Niño with off-equatorial westerly wind events, Clim Dyn doi:10.1007/s00382-015-2891-8. doi:10.1007/s00382-015-2891-8

McPhaden MJ, Zebiak SE, Glantz MH (2006) ENSO as an integrating concept in earth science. Science 314(5806):1740–1745. doi:10.1126/science.1132588

Meehl GA, Arblaster JM, Loschnigg J (2003) Coupled ocean-atmosphere dynamical processes in the tropical Indian and Pacific Ocean regions and the TBO. J Clim 16:2138–2158. doi:10.1175/2767.1

Meinen CS, McPhaden MJ (2000) Observations of warm water volume changes in the equatorial Pacific and their relationship to El Niño and La Niña. J Clim 13:3551–3559

Neske S, McGregor S (2018) Understanding the Warm Water Volume Precursor of ENSO Events and its Interdecadal Variation. Geophys Res Lett 45:1577–1585. doi: 10.1002/2017GL076439

Palanisamy H, Cazenave A, Delcroix T, Meyssignac B (2015) Spatial trend patterns in the Pacific Ocean sea level during the altimetry era: the contribution of thermocline depth change and internal climate variability. Ocean Dyn *65*(3):341-356. doi:10.1007/s10236-014-0805-7

Petrova D. Koopman SJ, Ballester J, Rodó X (2017) Improving the long-lead predictability of El Niño using a novel forecasting scheme based on a dynamic components model. Clim Dyn 48(3-4):1249-1276. doi:10.1007/s00382-016-3139-y

Philander SGH, Pacanowski RC (1980) The generation of equatorial currents. J Geophys Res 85(C2):1123-1136

Picaut J, Masia F, du Penhoat Y (1997) An advective-reflective conceptual model for the oscillatory nature of the ENSO. Science 277:663–666. Doi:10.1126/science.277.5326.663

Puy, M, Vialard J, Lengaigne M, Guilyardi E, DiNezio PN, Voldoire, A, Mcphaden MJ (2017) Influence of Westerly Wind Events stochasticity on El Niño amplitude: the case of 2014 vs. 2015. Clim Dyn 1-20. doi:10.1007/s00382-017-3938-9

Ramesh N, Murtugudde R (2013) All flavours of El Niño have similar early subsurface origins. Nature climate change 3(1):42-46. doi:10.1038/nclimate1600

Rayner NA, Parker DE, Horton EB, Folland CK, Alexander LV, Rowell DP, Kent EC, Kaplan A (2003) Global analyses of sea surface temperature, sea ice, and night marine air temperature since the late nineteenth century. J Geophys Res 108(D14):4407. doi:10.1 029/2002JD002670

Rebert JP, Donguy JR, Eldin G, Wyrtki K (1985) Relations between sea level, thermocline depth, heat content, and dynamic height in the tropical Pacific Ocean. J Geophys Res *90*(C6):11719-11725

Ruiz JE, Corder, I, Sharma A. (2005) Integrating ocean subsurface temperatures in statistical ENSO forecasts. J Clim *18*(17):3571-3586. doi:10.1175/JCLI3477.1

Smith NR (1995) An improved system for tropical ocean subsurface temperature analyses. J Atm Ocean Tech *12*(4):850-870

Shu L, Clarke AJ (2002) Using an ocean model to examine ENSO dynamics. J Phys Oceanogr *32*(3):903-923

Suarez MJ, Schopf PS (1988) A delayed action oscillator for ENSO. J Atmos Sci 45:3283–3287

Suresh I, Vialard J, Lengaigne M, Han W, McCreary J, Durand F, Muraleedharan PM (2013) Origins of wind-driven intraseasonal sea level variations in the North Indian Ocean coastal waveguide. Geophys Res Lett. doi:10.1002/2013GL058312

Suresh I, Vialard J, Izumo T, Lengaigne M, Han W, McCreary JP, Muraleedharan PM (2016) Dominant role of winds near Sri Lanka in driving seasonal sea level variations along the west coast of India. Geophys Res Lett. *43*(13):7028-7035. doi:10.1002/2016GL069976

Takahashi K, Montecinos A, Goubanova K, Dewitte B (2011) ENSO regimes: reinterpreting the canonical and Modoki El Niño. Geophys Res Lett 38:1–5. doi:10.1029/2011GL047364

Taylor KE, Stouffer RJ, Meehl GA (2012) An overview of CMIP5 and the experiment design. Bull Am Meteorol Soc *93*(4):485-498. doi:10.1175/BAMS-D-11-00094.1

Thual S, .Dewitte B, Ayoub N, Thual O (2013) An asymptotic expansion for the recharge-discharge model of ENSO. J Phys Oceanogr 43:1407–1416. doi:10.1175/JPO-D-12-0161.1

Torrence C, Webster PJ (1998) The annual cycle of persistence in the El Nño/Southern Oscillation. Q J R Meteorol Soc *124*(550):1985-2004

Vialard J, Menkes C, Boulanger J-P, Delecluse P, Guilyardi E, McPhaden M (2001) A model study of the oceanic mechanisms affecting the equatorial SST during the 1997–98 El Niño. J Phys Oceanogr 31:1649–1675

Wen C, Kumar A, Xue Y, McPhaden MJ (2014) Changes in tropical Pacific thermocline depth and their relationship to ENSO after 1999. J Clim *27*(19):7230-7249. doi:10.1175/JCLI-D-13-00518.1

Wyrtki K (1985) Water displacements in the Pacific and the genesis of El Niño cycles. J Geophys Res 90:7129–7132

Yu Y, Dommenget D, Frauen C, Wang G, Wales S (2016) ENSO dynamics and diversity resulting from the recharge oscillator interacting with the slab ocean. Clim Dyn *46*(5-6):1665-1682. doi:10.1007/s00382-015-2667-1

Zelle H, Appeldoorn G, Burgers G, van Oldenborgh GJ (2004) The relationship between sea surface temperature and thermocline depth in the eastern equatorial Pacific. J Phys Oceanogr *34*(3):643-655. doi:10.1175/2523.1

Zhang Q, Kumar A, Xue Y, Wang W, Jin FF (2007) Analysis of the ENSO cycle in the NCEP coupled forecast model. J Clim *20*(7):1265-1284. doi:10.1175/JCLI4062.1

Zhang X, Clarke AJ (2017) On the dynamical relationship between equatorial Pacific surface currents, zonally-averaged equatorial sea level and El Niño prediction. J Phys Oceanogr **47(2)**:323-337

Zhu X, Greatbatch RJ, Claus M (2017) Interannual variability of tropical Pacific sea level from 1993 to 2014, J Geophys Res Oceans 122:602–616. doi:10.1002/2016JC012347

TABLE AND FIGURES

	baroc. 1	baroc. 2	baroc. 3	K_{1+2}+$R1_{1+2}$	Residual = Total - K_{1+2}-$R1_{1+2}$
WWV_W	58%	33%	9%	86%	14%
WWV_E	53%	36%	11%	96%	4%
WWV	69%	26%	5%	99%	1%

Table 1 : % of contribution obtained from the regression coefficient of each contribution onto total signal, for each index, in the historical LCS experiment forced by 20CR windstress.

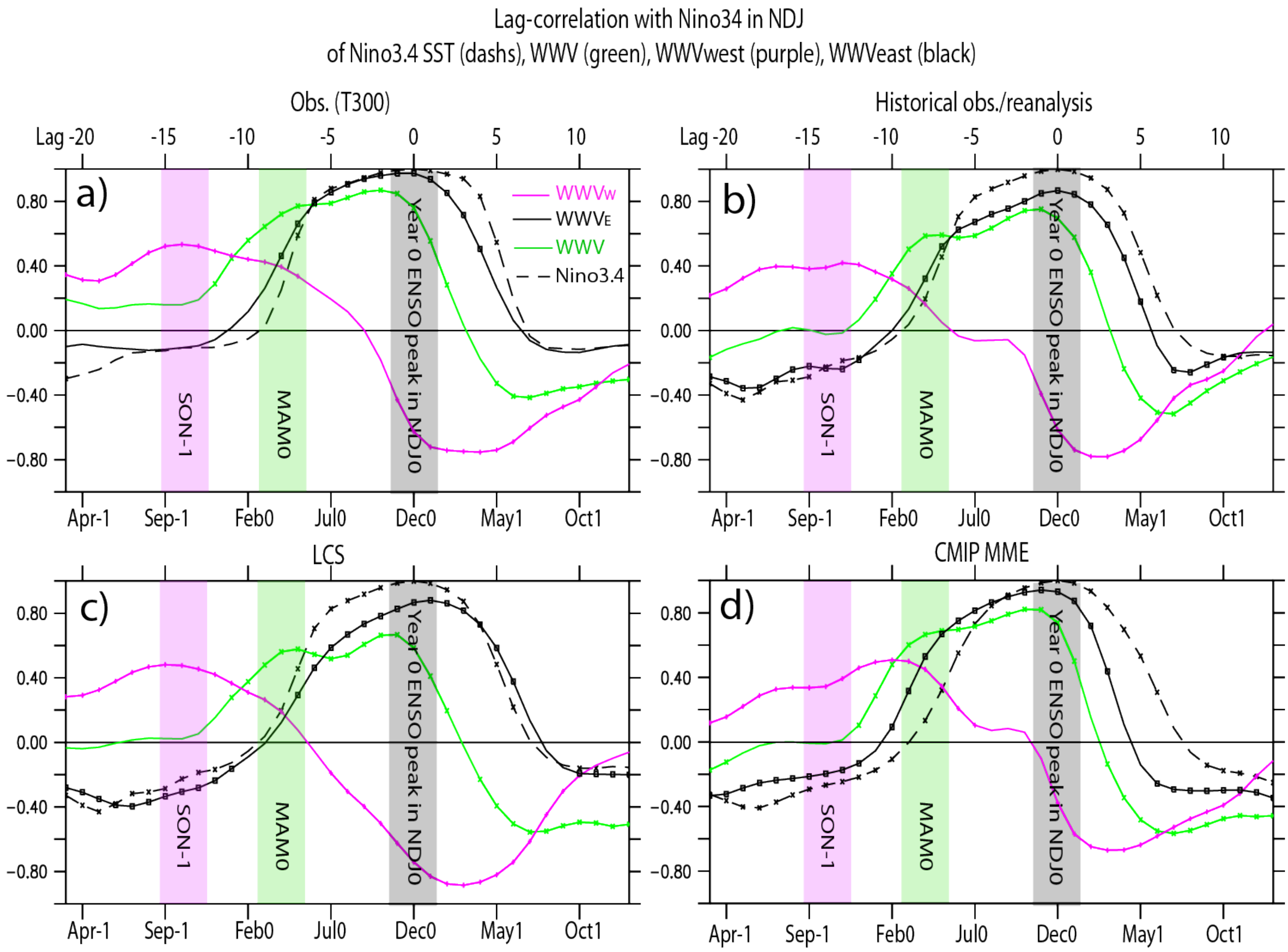

Fig. 1. Lead-lag correlation of WWV indices with ENSO peak. (a) Lag-correlation of TAO/TRITON/BMRC T300-based WWV_W (purple), WWV_E (black) and WWV (green), as well as Niño34 SST (dashed black) with Niño3.4 SST in NDJ_0 (in the entire paper, the index makes reference to the central month of the period, with 0 designating the year of the ENSO onset and growth, and -1 and 1 the previous and next years respectively) over the 1980-2017 period. Negative lags (in months) mean that e.g. WWV leads Niño3.4 index. (b) Same as (a) but for SLA-based WWV from historical observations/reanalysis over the 1900-2008 period. (c) Same as (b), but for 20CRv2 LCS simulation over the 1900-2008 period. d) Same as b, but for CMIP MMM (Multi-Model Mean) for historical runs over the 1861-2005 period (here the multi-model mean of the lag-correlation computed for each model separately is shown). Correlations that are different from zero at the 90% confidence level for observations/reanalysis and LCS, and the 70% sign consistency level for CMIP MMM, are marked using crosses/dots. Shaded purple, green and grey vertical bars respectively highlight SON_{-1}, MAM_0 and NDJ_0 .

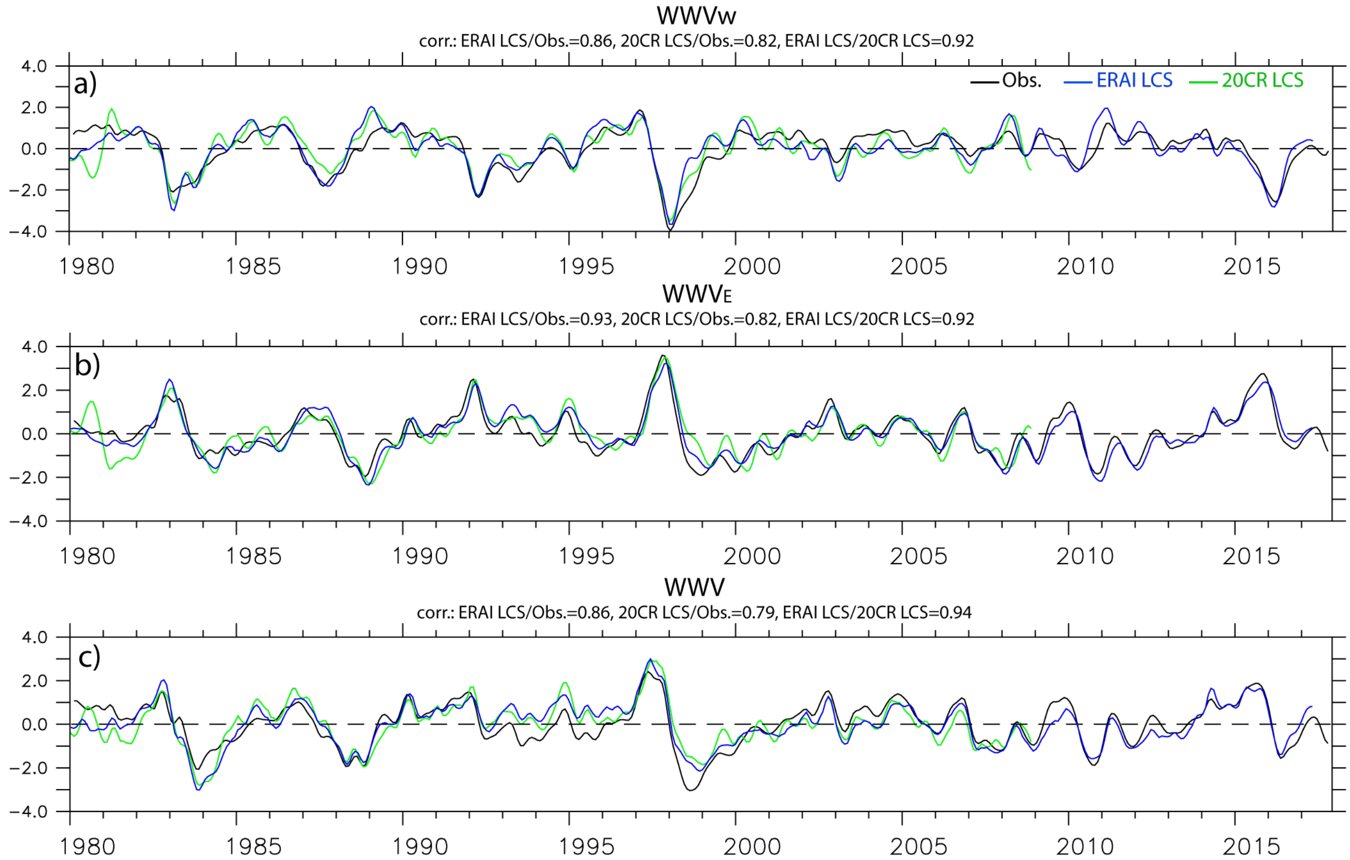

Fig. 2. Validation of LCS WWV indices. Anomalous time series for normalised (a) WWV_W, (b) WWV_E and (c) WWV based on T300 from TAO/TRITON/BMRC (black) and based on SLA from ERA-I (blue) or 20CR (green) wind-forced LCS experiments. All time series are linearly detrended. Correlations between each of the three datasets are given on the top of each panel.

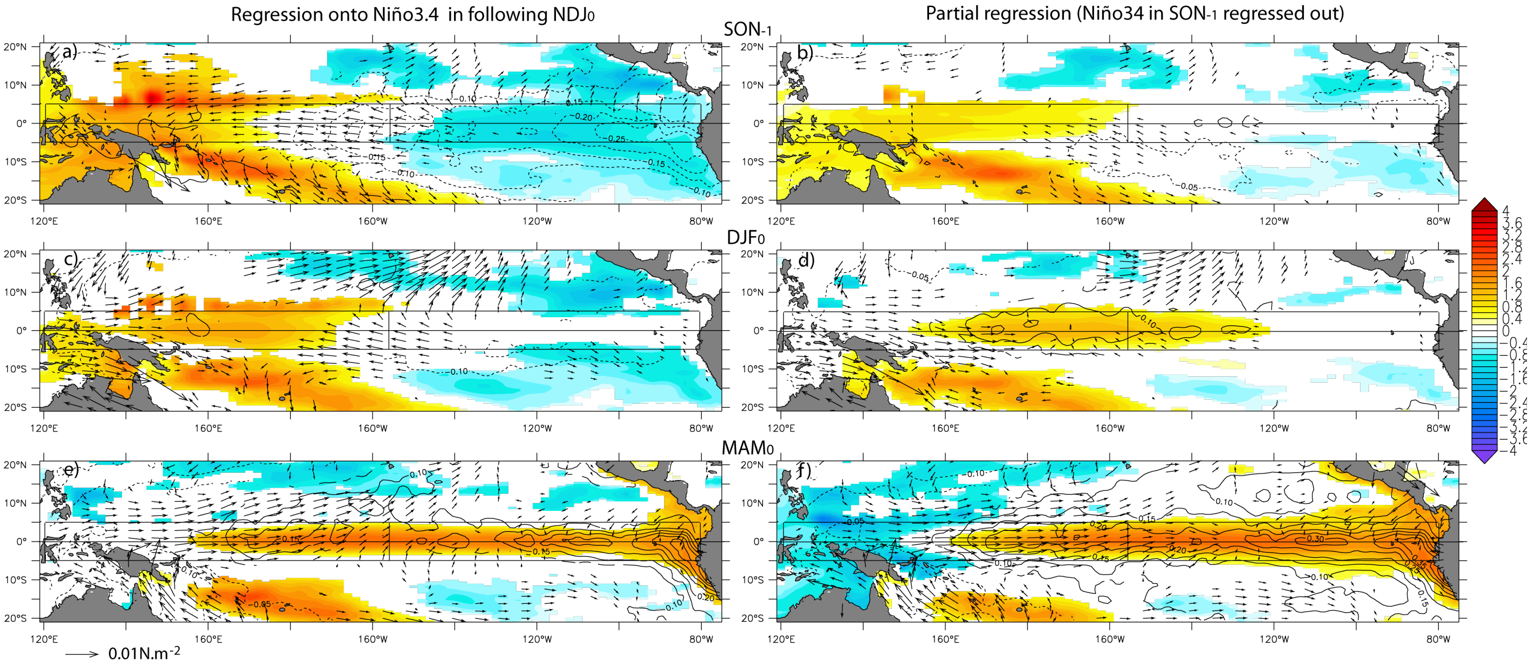

Fig. 3. Precursory SLA signals before and during ENSO onset. (Top) SON$_{-1}$, (middle) DJF$_0$ (Dec$_{-1}$ to Feb$_0$), (bottom) MAM$_0$ SLA (color), SSTA (SST anomalies, contours) and wind stress anomalies (vectors) regressed onto normalized NDJ$_0$ (Nov$_0$ to Jan$_1$) Niño3.4 SSTA in SODA reanalysis. Left panels correspond to simple regression analyses while right panels display partial regressions, in which previous year's ENSO influence has been removed (i.e. signals independent of the influence of Niño3.4 in SON$_{-1}$). Units are cm for SLA, ˚C for SSTA and N.m^{-2} for wind stress. Signals are shown only if they are statistically significant at the 90% level. Boxes defining WWV indices, and equator, are shown in black.

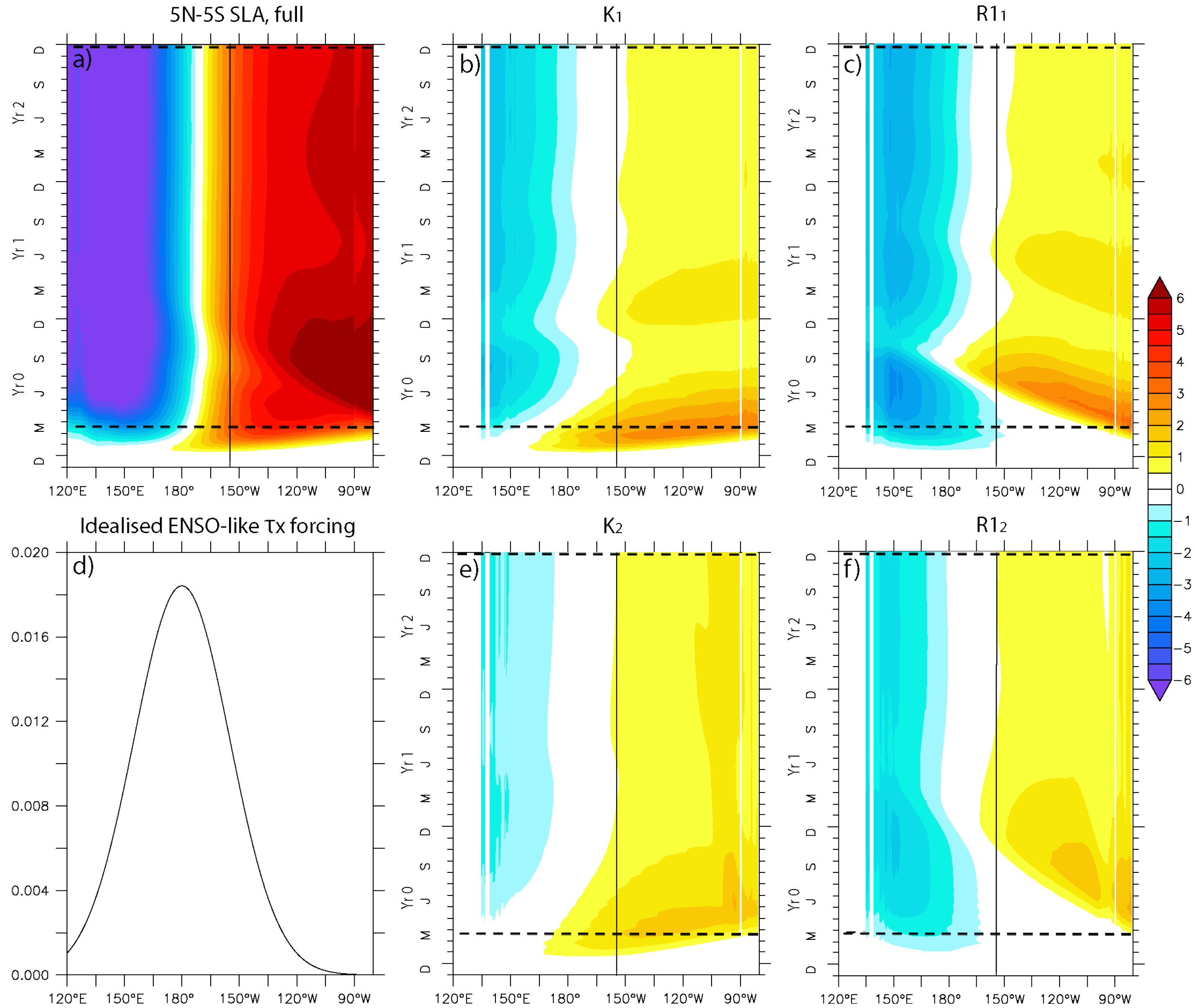

Fig. 4. Equatorial longitude-time SLA evolution for the idealized LCS switch-on westerlies experiment. (a) Equatorial (5°N-5°S) SLA from idealized LCS experiment (in cm). Contribution from **b)** K_1, **c)** $R1_1$, **e)** K_2, **f)** $R1_2$ to the SLA signal shown in panel a. The vertical line indicates the boundary between the WWV_E and WWV_W boxes. The horizontal dashed lines indicate the dates (after 2.5 months and 3 years) of the snapshots in Figure 5bc. (d) Gaussian zonal profile of the zonal wind stress forcing for this idealized experiment starting from January, Yr0 averaged over 5°N-5°S.

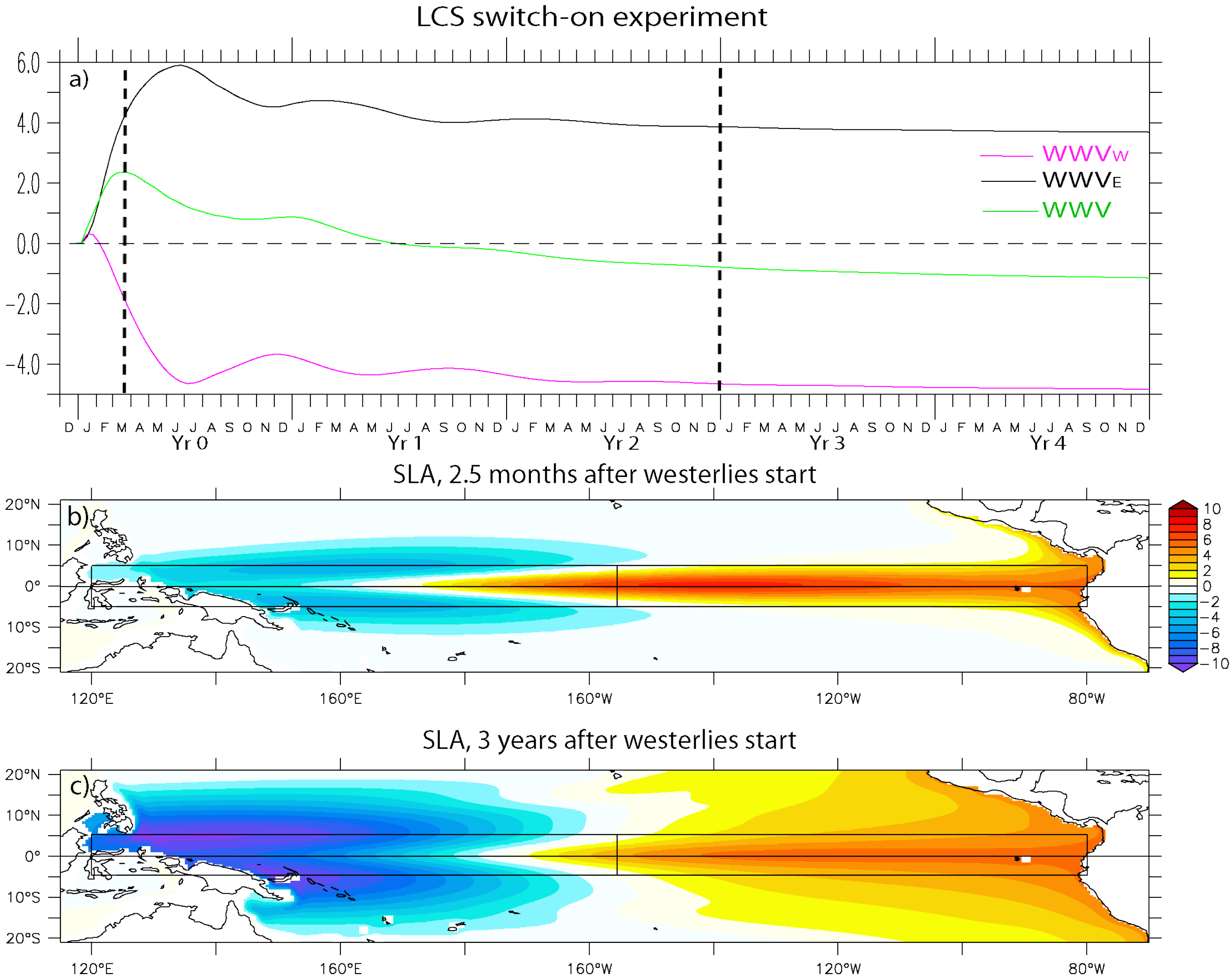

Fig. 5. Response of the WWV indices in the idealised LCS switch-on westerlies experiment. (a) Temporal evolution of WWV (green), WWV_E (black), WWV_W (purple). (b) SLA snapshot at the time of the maximum of the WWV temporary recharge, i.e. 2.5 months after westerlies are switched on. (c) Same as (b) but when the quasi-stationnary state has been reached in the equatorial band, i.e. 3 years after westerlies are switched on. Units are in cm for SLA maps and in 10^{13} cm.m^2 for WWV indices. Boxes of these indices, and equator, are shown in black.

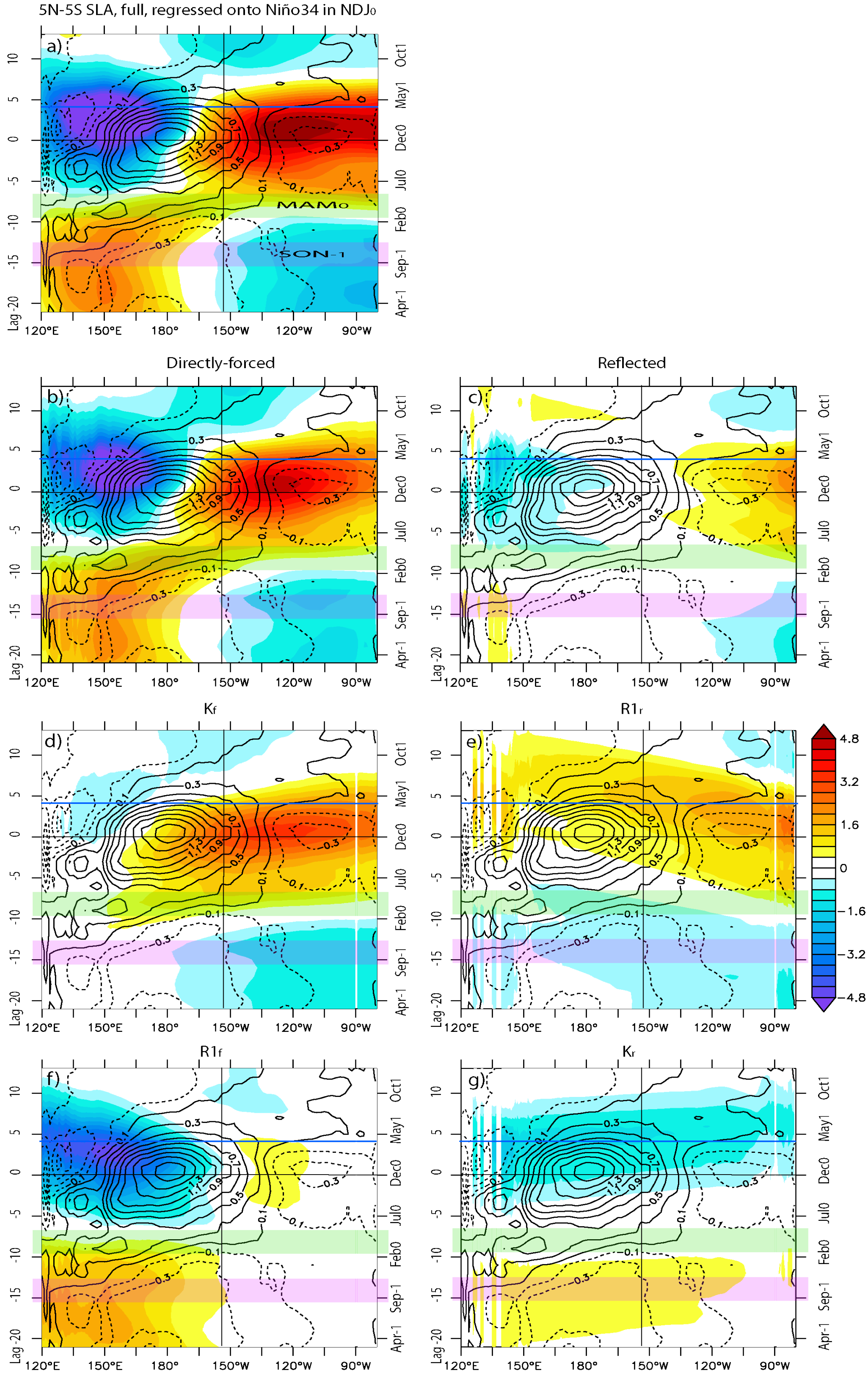

Fig. 6. Lag-regression onto normalised Niño3.4 SST in NDJ0 for (a) the total 5°S-5°N 20CR LCS SLA (cm, colors) during 1900-2008**,** the contributions from the **(b)** forced and **(c)** reflected signals, **(d)** the forced $K_{1+2,f}$, **(e)** its reflection at the eastern boundary into reflected $R1_{1+2,r}$, **(f)** forced $R1_{1+2,f}$ and **(g)** its reflection at the western boundary into reflected $K_{1+2,r}$. In all panels, zonal windstress (in $10^{-2}N/m^2$) is overlaid as black contours. The vertical axis denotes the lag in months (same convention as in Fig. 1). Vertical dashed lines represent the 155°W boundary between WWV_W and WWV_E regions. Shaded pink highlights SON_{-1}, shaded green shows MAM_0. Blue horizontal line represents next MAM_1, when ENSO event and related westerlies have terminated.

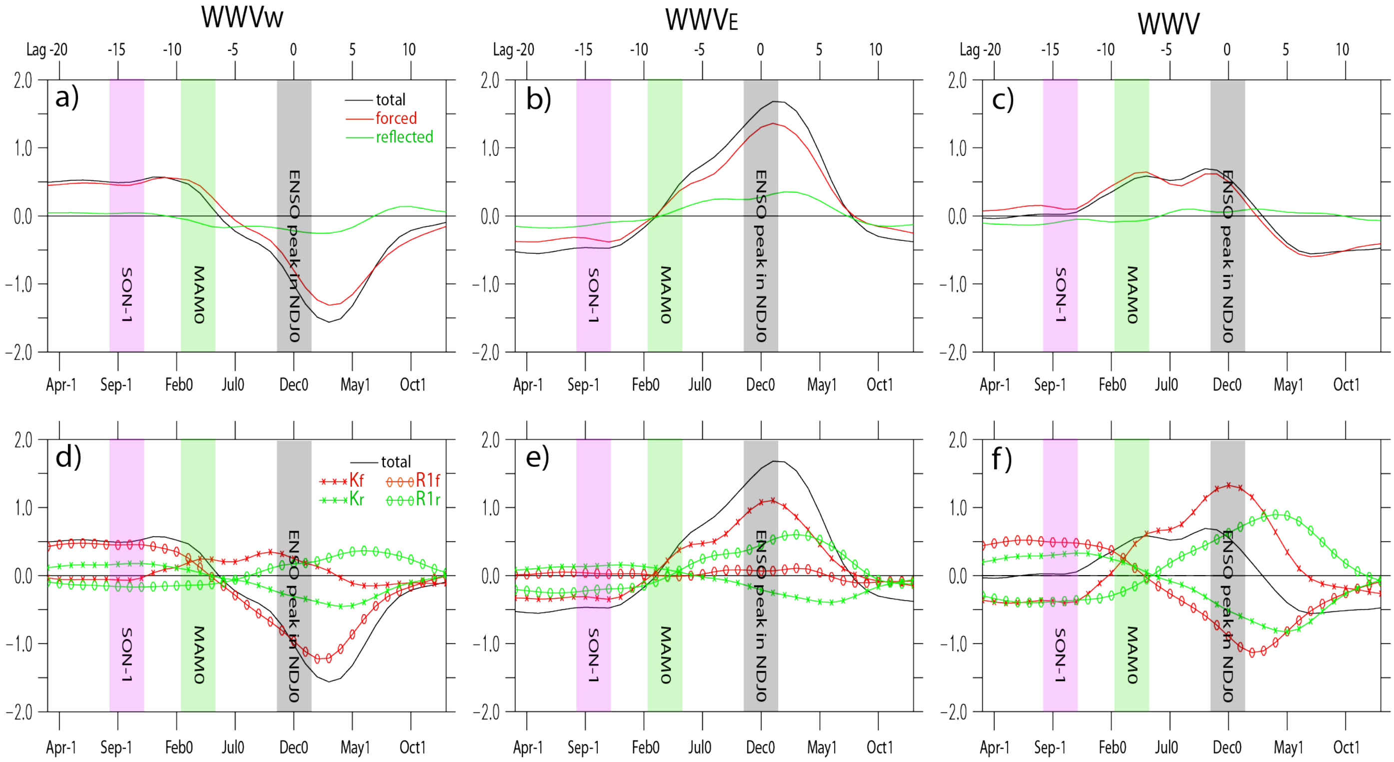

Fig. 7. Contribution of directly-forced and reflected waves to all three WWV indices. Lag-regression onto normalised ENSO index of (left) WWV_W, (middle) WWV_E and (right) WWV (full in black) and the respective contribution of the directly-forced (red) and reflected (green) signals (upper panels), further decomposed into K_{1+2} (crosses) and $R1_{1+2}$ (circles) in the lower panels. Based on 20CR-forced LCS. All curves divided by the full WWV STD (thus, left+middle columns curves = right column curves).

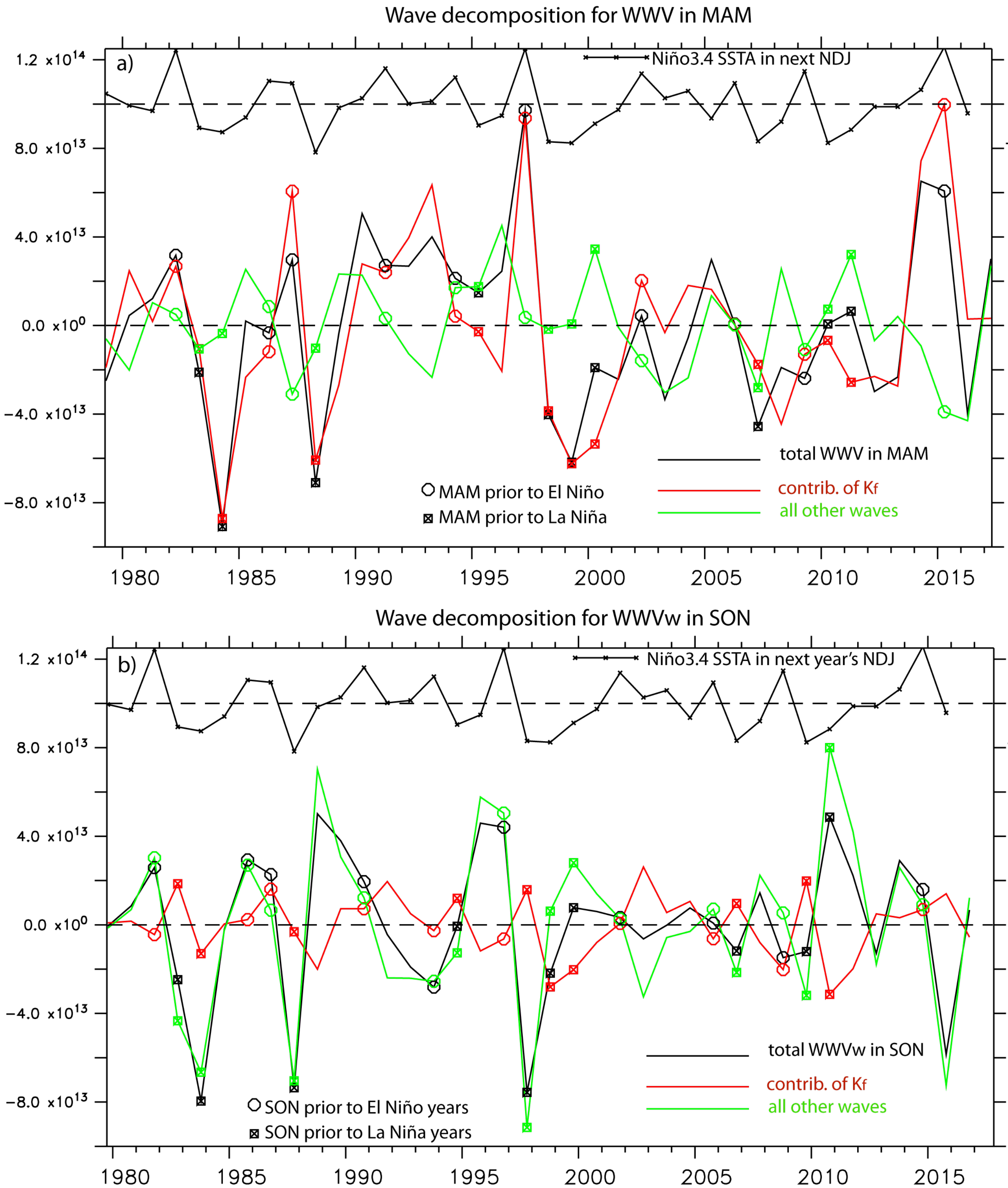

Fig. 8. The main wave contributions to recent variations of (a) WWV in MAM and (b) WWV$_W$ in SON. a) ERAI-forced LCS WWV in MAM, and the contributions of K_f (i.e. rapid oceanic response; red) and all other waves (i.e. slower oceanic response, the residual WWV-K_f; green). Values during El Niño years are highlighted as circles, and La Nina years as squares. Time series of Niño3.4 SST in following NDJ is shown as an inset on the top of each panel (black line with crosses; SST levels in ^oC are shown on right vertical axis), shifted backward by 8 months to match the MAM values. b) same for WWV$_W$ in SON; Niño3.4 SST is shifted here by 14 months (e.g., in panel b, the Nov.1997-Jan.1998 value of Niño3.4 is shown on SON 1996).

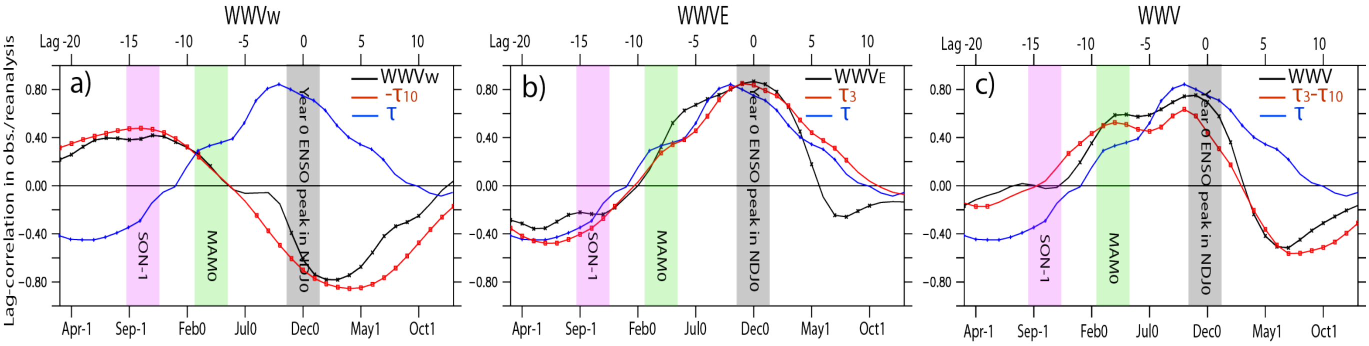

Fig. 9. Lead-lag correlation as Fig. 1b (historical observations/reanalysis), but now **with the different wind forcing terms explaining the WWV_W (left column), the WWV_E (middle) and the WWV (right). a)** WWV_W (black) and **-**τ_{10} (red). **b)** WWV_E (black) and τ_3 (red). **c)** WWV (black) and $\tau_3 - \tau_{10}$ (red, cf. equation 3). Equatorial Pacific τ_x is shown in all panels for reference (blue).

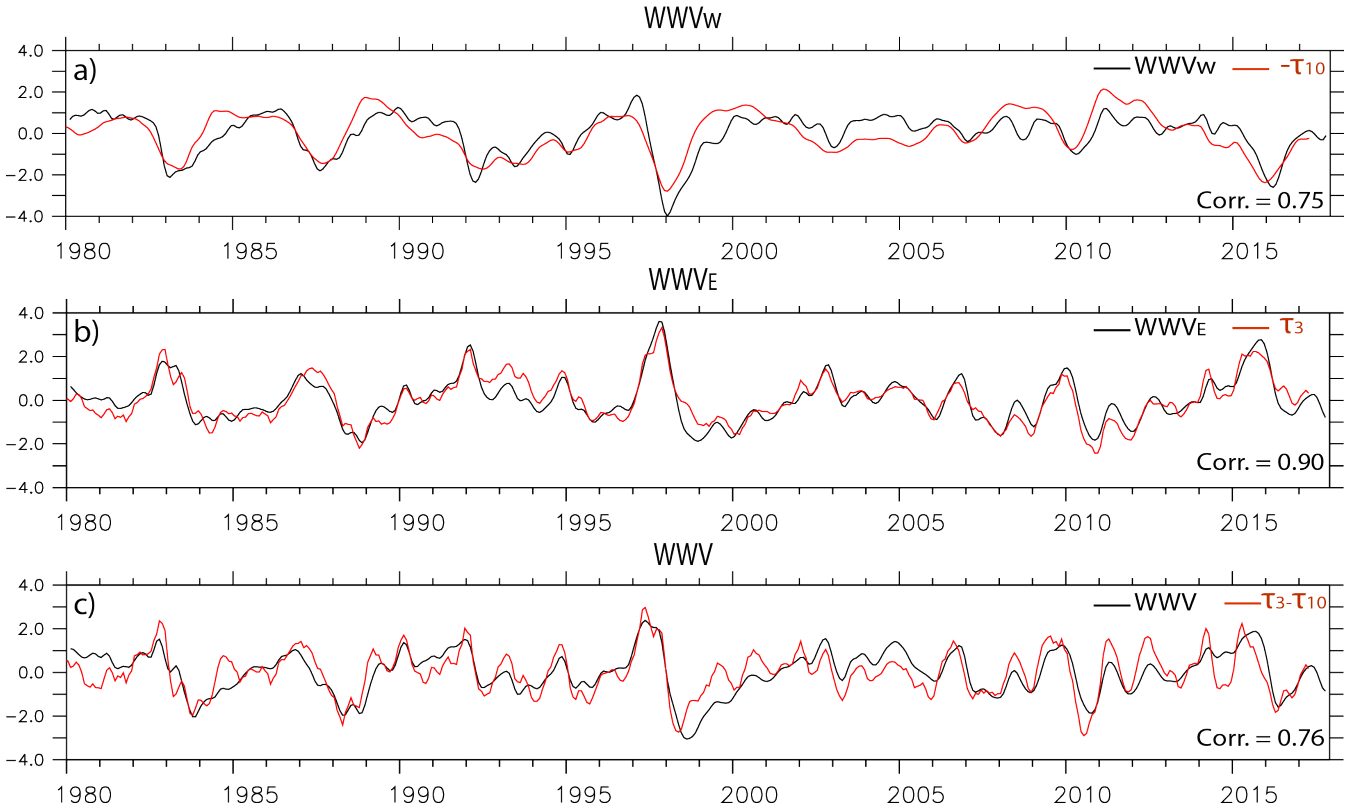

Fig. 10. Explaining recent observed WWV indices variations with the wind forcing terms. Anomalous time series of normalised WWV_W, WWV_E and WWV from TAO/TRITON/BMRC T300 observations (black), and their related normalised wind proxies (red, from ERAI): a) $-\tau_{10}$; b) τ_3; c) $\tau_3 - \tau_{10}$ (correlation given within each panel). All time series are detrended.

On the physical interpretation of the lead relation between Warm Water Volume and the El Niño Southern Oscillation

SUPPLEMENTARY INFORMATION

Takeshi Izumo (1,2), Matthieu Lengaigne (1,2), Jérôme Vialard (1), Iyyappan Suresh (3), and Yann Planton (1)

(1) LOCEAN-IPSL, Sorbonne Université (UPMC, Université Paris 06)- CNRS-IRD-MNHN, Paris, France

(2) Indo-French Cell for Water Sciences, IISc-NIO-IITM-IRD Joint International Laboratory, CSIR-NIO, Goa, India

(3) CSIR-National Institute of Oceanography, Goa, India

Boundary conditions used within the LCS to separate directly-forced and reflected waves

To separate quantitatively the directly-forced and reflected equatorial waves, we have conceived an additional LCS experiment with dampers (dampers defined as in e.g. McCreary et al. 1996, Suresh et al. 2016). The sensitivity experiments with "no reflections" apply dampers from 65°S to 65°N over areas which are normally land in the control experiment, i.e. west of 120°E and east of 80°W. The damping coefficient is ramped at the land-sea boundary in order to avoid numerical instabilities. The control experiment minus the "no reflection" experiment provides an estimate of reflected signals. In order to demonstrate that this simple approach successfully separates the forced and reflected signals, we show the results of the decomposition in Figure S1 below, for an idealised experiment with a short wind burst applied in the central Pacific. As can be seen in panel c, the reflected contributions look exactly as they are supposed to look, confirming that our approach to separate reflected signals is appropriate.

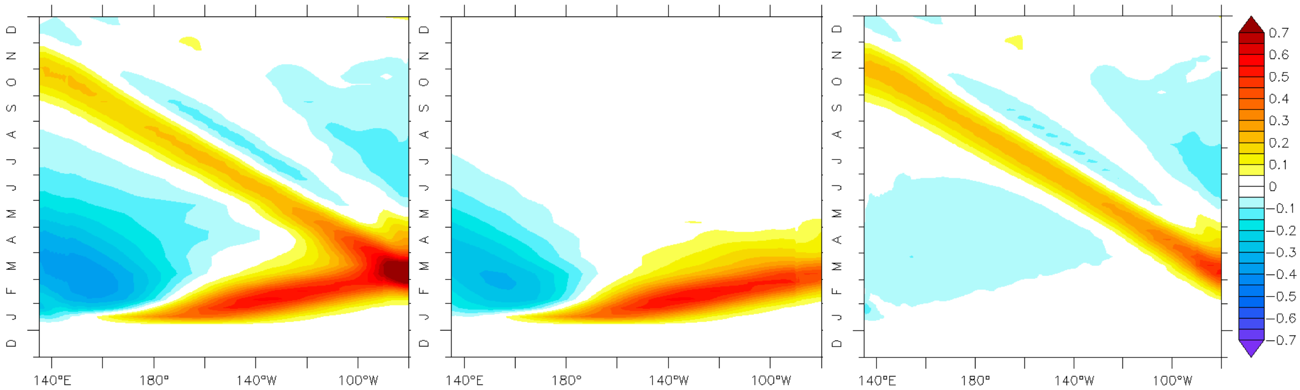

Figure S1: Hovmüller of the SLA response (cm) averaged over 5°N-5°S to an idealised westerly pulse lasting 10 days, in early January (same Gaussian spatial pattern as the one described in Fig. 4d) for (left) the full experiment, (middle) the experiment with no wave reflection (i.e. with dampers at both western and eastern boundaries) and (right) their difference (i.e. the reflected signals).

Main message: The forced and reflected waves look similar to the expected theoretical solution, underlining the relevance of the method to separate the forced and reflected contributions.

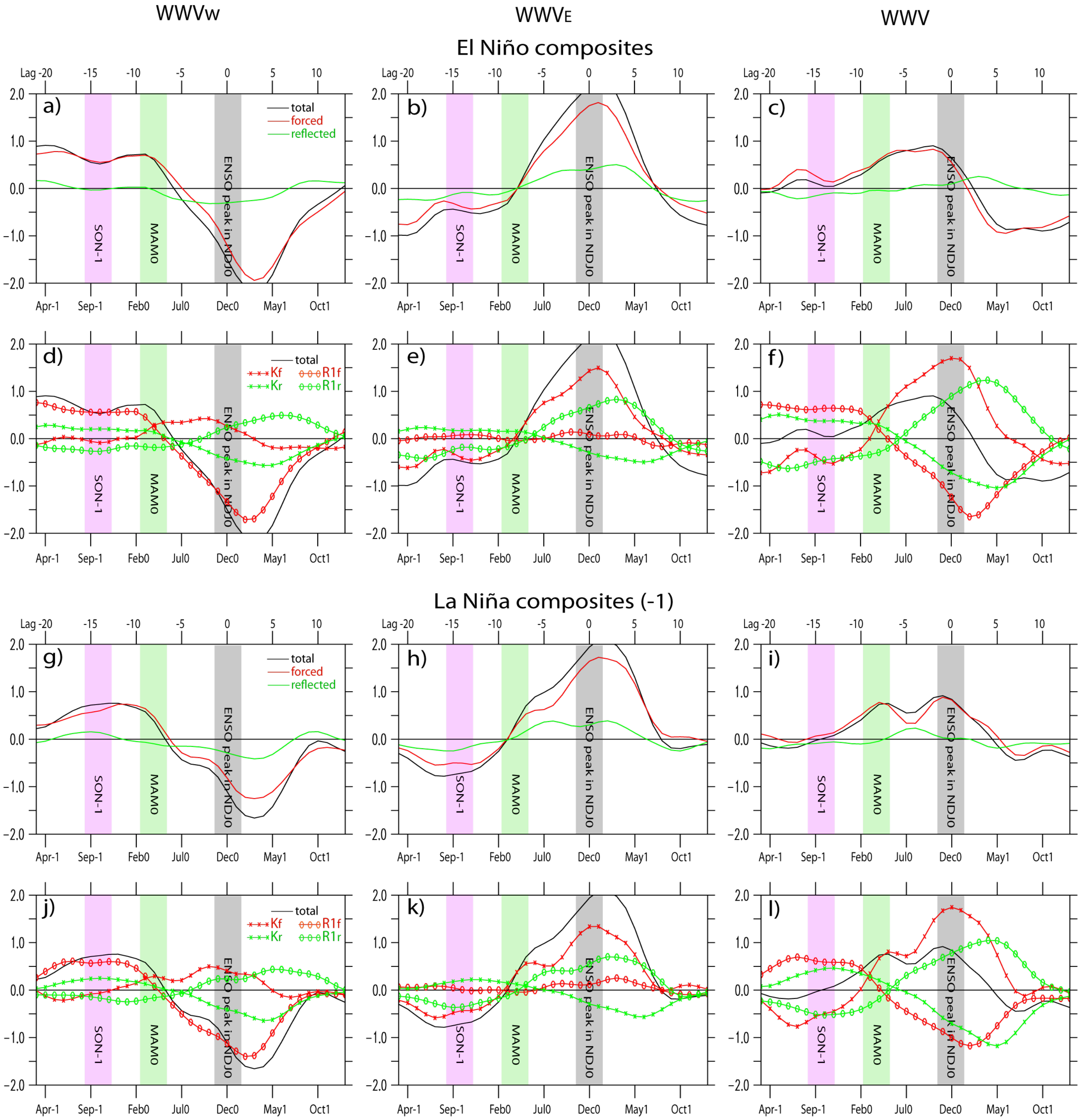

Figure S2. Equivalent to Fig. 7, but for El Nino composites (1st and 2nd rows) **and La Nina composites** (with a -1 sign, for easier comparison; 3rd and 4th rows). Years are defined as El Niño or La Niña when Niño3.4 SST anomaly in NDJ is larger than 2/3 of its interannual standard deviation STD, i.e. approximately the quartile on each side of the distribution).

Main message: the results remain at first order valid for both ENSO phases, in observations as well as in CMIP MME (not shown), with only some 2nd order assymetries. Notably, the slow western Pacific recharge/discharge preconditionning tends to be sligthly stronger before a La Niña, implying that El Niño is harder to predict than La Niña from WWV_W, but is still mostly due to $R1_f$. At the end of an El Niño, the western Pacific discharge tends to be stronger than the recharge at the end of a La Niña event (but still mostly due to $R1_f$), and the WWV has a larger and earlier sign reversal due to a larger $R1_f$ contribution counteracting K_f, likely because the El Niño westerly anomaly is stronger than the La Niña easterly one. We are currently investigating in more details these asymmetries, likely larger for extreme events (Planton et al., in prep.).

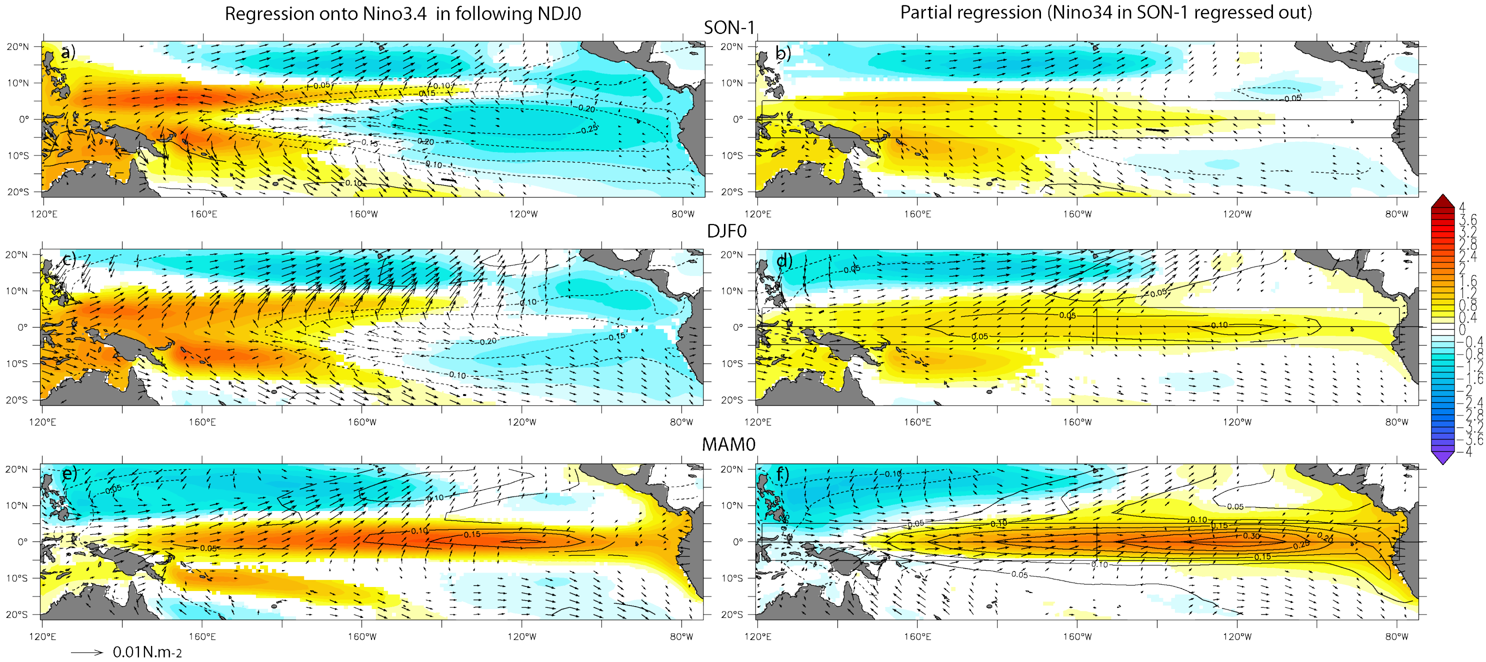

Fig. S3. As Fig. 3 (SLA in colors, SST in black contours), **but for CMIP MMM**. Signals only shown when sign is consistent in at least 70% of the CMIP models.

Main message: CMIP5 simulations agree qualitatively well with observations, which reaffirms that the processes controlling the SLA are generally similar in these climate models.

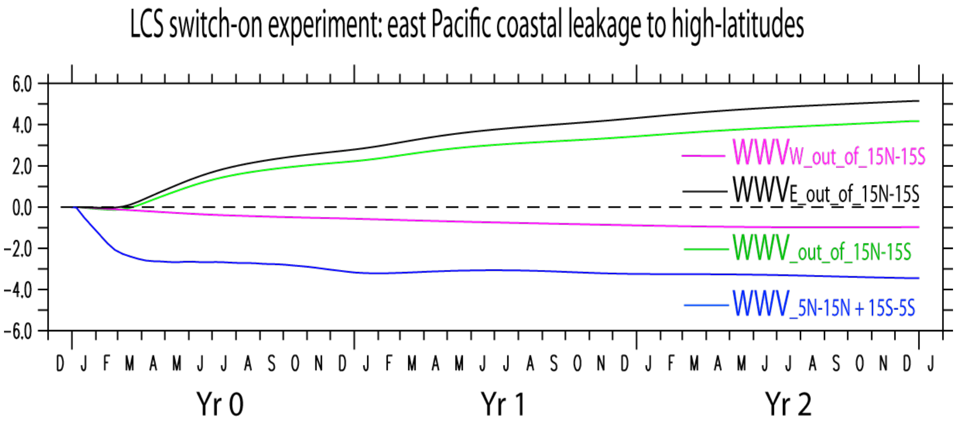

Fig. S4. Role of leakage to high-latitudes for WWV long-term recharge/discharge. As Fig. 5a, i.e. for the idealised LCS switch-on westerlies experiment, but here for WWV within the 15°N-15°S band excluding the equatorial 5°N-5°S band (i.e. 15°S-5°S plus 5°N-15°N bands, blue), all WWV out of 15°N-15°S band (green) and its west (purple) and east (of 155°W, black, including WWV gone to Atlantic) contributions.

Main message: understanding such idealised switch-on experiment - which is exactly the temporal integral of the impulse response shown in Izumo et al. (2016) thanks to linearity - is important for understanding the fundamental processes at play. The oceanic response to any temporal evolution of the ENSO-like τ_x pattern will be exactly the convolution with the LCS impulse response, thanks to LCS linearity (and to the quasi-linearity of ocean dynamics for the processes analysed here; e.g. Izumo et al. 2016).

Suppl. Fig. S4 shows that ***the long-term recharge/discharge of the equatorial band is due to leakage to subtropics and mid-latitudes through the east Pacific coastal waveguides***, in the switched-on westerlies idealised experiment. The WWV within the 15°N-15°S band excluding the equatorial 5°N-5°S band, in blue, shows a long-term *discharge* in the case of switched-on *westerlies*, while the *contrary* would be expected if the long-term discharge of the equatorial band WWV were due to meridional Sverdrup transport at 5°N and 5°S, as hypothesized by Jin et al. (1997ab), or to Rossby waves forcing near the equator (Zhu et al. 2017). The long-term recharge explaining the equatorial band discharge is actually out of the 15°N-15°S band, and in the east Pacific only, and is caused by the leakage to subtropics and mid-latitudes through the east Pacific coastal waveguides (poleward coastal Kelvin waves, and the Rossby waves then emited westward along their path, cf. Fig. 5c; a leakage ~2 times larger towards the south of 15°S than to the north of 15°N; not shown), as suggested by the original recharge theory of Wyrtki (1985). Hence, the long-term discharge after 5 years, when measured over a wider 15°N-15°S tropical band (as in Wyrtki 1985), is ~5 times larger than the usual 5°N-5°S WWV, and completely dominates the temporal evolution of “tropical 15°N-15°S WWV”. These results further question the relevance of using the usual WWV for the recharge oscillator paradigm.

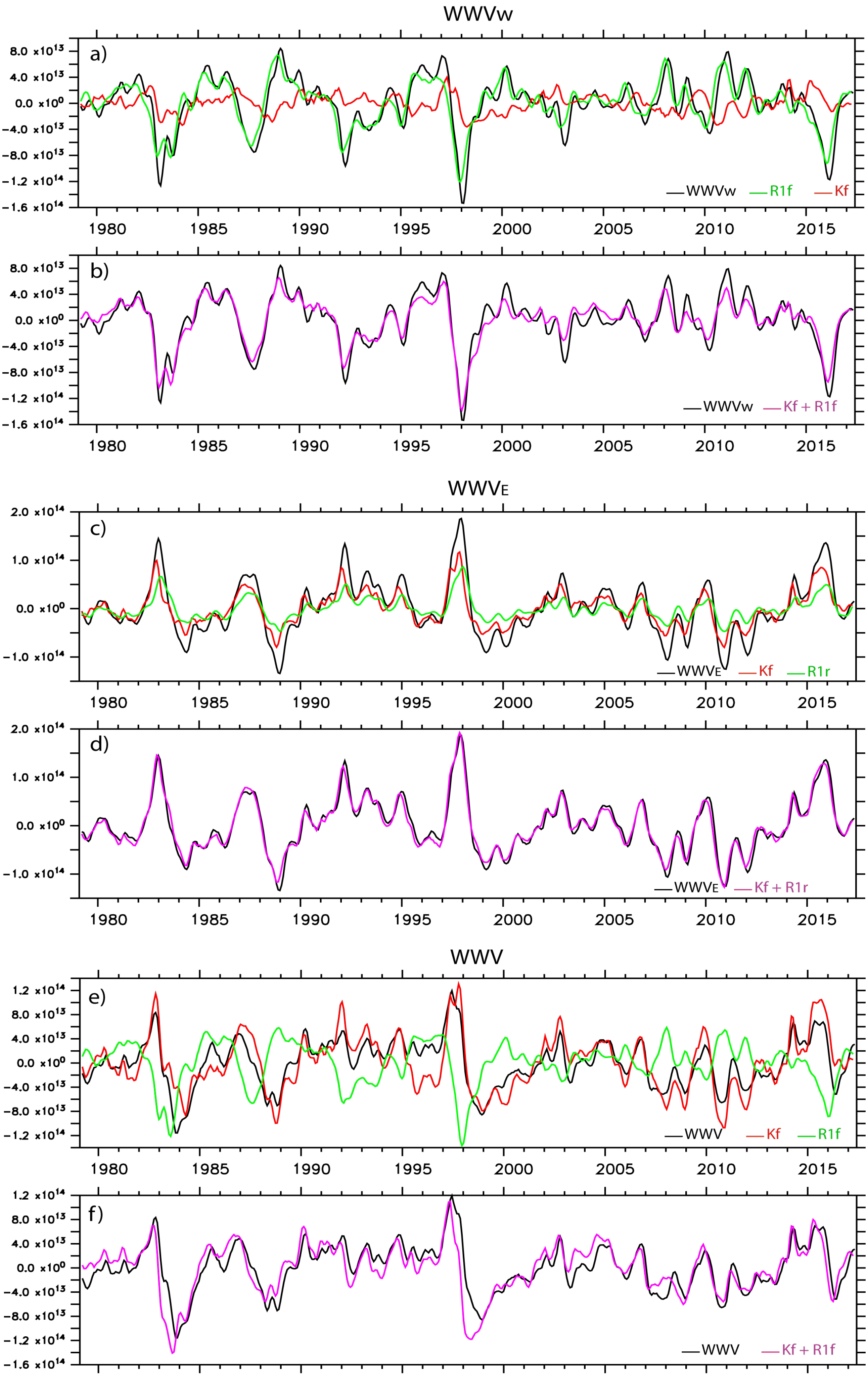

Fig. S5. The waves dominating WWV_W, WWV_E and WWV. Time series of ERAI-LCS WWV indices (black), confirming the approximations (purple; each wave separately in red/green) chosen in section 3.3.

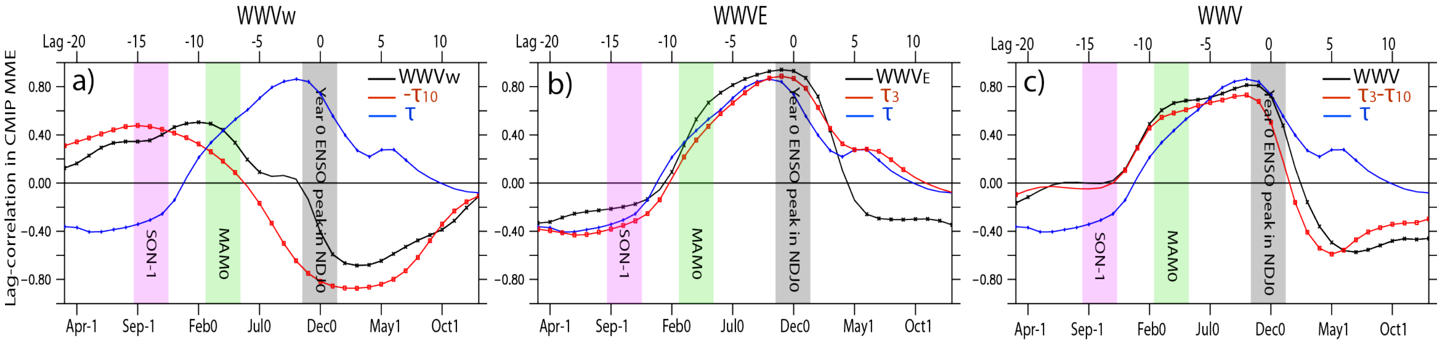

Fig. S6. As Fig. 9, but for CMIP MMM. Crosses/dots only shown when sign is consistent in at least 70% of the CMIP models.

Main message: for CMIP MMM, there is also a qualitative agreement between the WWV indices and their respective wind forcing. It is however slightly less accurate than that for observations. E.g. the actual WWV_W decreases later than WWV_W wind proxy, $-\tau_{10}$, during ENSO onset. This mismatch is certainly related with the tendency of most CMIP models to exhibit a typical cold tongue bias and related westward shift of ENSO-related wind stress (e.g. Bellenger et al. 2013, Brown et al. 2014). The westerly-induced downwelling K_f at ENSO onset is then shifted to the west (cf. Suppl. Fig. S3) compared to observations, having thus more weightage on the WWV_W box and competing more with upwelling $R1_f$ wave. There is another mismatch, between WWV_E and its proxy τ_3 during ENSO decay phase, maybe because the negative contribution of the upwelling reflected Kelvin wave K_r to WWW_E is not well captured.

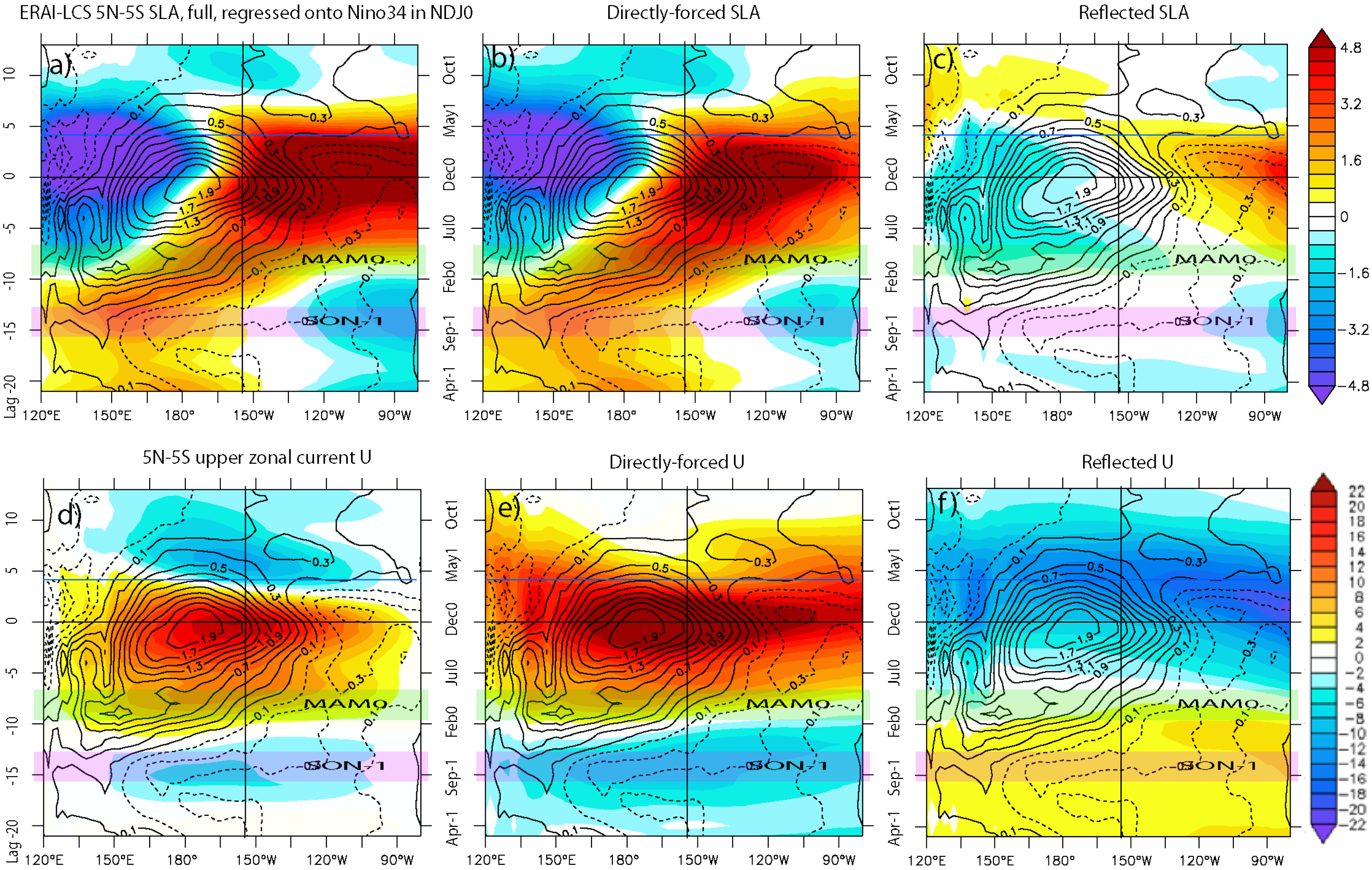

Fig. S7. Dominance of the zonal advection delayed negative feedback on the thermocline one. As Fig. 6a,b,c, but here for ERAI-forced LCS SLA (shading in upper panels, cm) and zonal current in the upper 100m (shading in lower panels, cm/s), and for ERAI zonal windstress (contours).

Main message :

Upper panels show that results remain similar for ERAI-forced LCS (1979-2017), as compared to 20CR-forced LCS over a much longer period (1900-2008, cf. Fig. 6), with slightly stronger amplitudes, due to stronger windstress (due possibly to the stronger El Nino events that occured in the recent period, and likely also to better observational constraints).

Comparing these upper panels with the lower ones for the upper layer zonal current U allows us to compare thermocline and zonal advection delayed negative feedbacks. Concerning the phase transition after an ENSO peak, e.g. an El Niño, upper panels suggest that the upwelling K_r effect on eastern Pacific thermocline depth, i.e. the delayed negative feedback at the heart of the delayed oscillator paradigm (Shopf and Suarez 1989, Battisti and Hirst 1989), is weak, being counteracted by the downwelling $R1_r$. The reversal of SLA anomaly only appears in central-eastern Pacific around lag +8 (i.e. JAS_{+1}), and is actually mainly due to K_f forced by the wind reversal. Conversely, there is a strong delayed negative impact of this downwelling $R1_r$ on U (with an additionnal, but weaker, effect of upwelling K_r on U), at the heart of the advective-reflective oscillator paradigm (Picaut et al. 1997), suggesting that this latter one may be generally dominant for short term delayed negative feedback on 5°N-5°S SST, rather than the original delayed oscillator (in agreement with earlier studies, e.g. Izumo et al. 2016), and hence for explaining the termination of an ENSO event. Concerning the ENSO onset (before spring, i.e. lag -10 and earlier), while the positive zonal currents related to $R1_r$ seem to play a favourable role, it is difficult, from our present analyses, to isolate its effect on SST from the WWV_W build-up effect, that could also play a role, possibly more through thermocline depth anomalies.

Additional discussion on the use of WWV in autumn as a precursor of following year's ENSO

One may wonder why WWV has still been a useful precursor in autumn (e.g. SON_{-1}) of following year's ENSO (e.g. Clarke and Van Gorder 2003, Izumo et al. 2010, 2014, Dayan et al. 2014, Jourdain et al. 2016), in apparent contradiction with the WWV non-significant correlation in SON_{-1} shown in Fig. 1. Actually, for the OHC component independent of the zonal tilt mode, Fig. 3b shows that the WWV region, in SON_{-1}, still captures part of the long-term preconditionning. Hence, when WWV is combined with the Indian Ocean Dipole (itself correlated with ENSO and the zonal tilt mode, not shown) through linear regression in these previous studies, it is actually this independent component of WWV that brings added predictability to the system (not shown).

Institute name	Model name
BCC	bcc-csm1-1
	bcc-csm1-1-m
CCCma	CanCM4
	CanESM2
CMCC	CMCC-CESM
	CMCC-CM
	CMCC-CMS
CNRM-CERFACS	CNRM-CM5
	CNRM-CM5-2
CSIRO-BOM	ACCESS1-0
	ACCESS1-3
CSIRO-QCCCE	CSIRO-Mk3-6-0
FIO	FIO-ESM
INM	inmcm4
IPSL	IPSL-CM5A-LR
	IPSL-CM5A-MR
	IPSL-CM5B-LR
LASG-CESS	FGOALS-g2
LASG-IAP	FGOALS-s2
MIROC	MIROC5
	MIROC-ESM
	MIROC-ESM-CHEM
MOHC	HadGEM2-CC
MRI	MRI-CGCM3
	MRI-ESM1
NASA-GISS	GISS-E2-R
	GISS-E2-R-CC
NCC	NorESM1-M
	NorESM1-ME
NOAA-GFDL	GFDL-CM2p1
	GFDL-CM3
	GFDL-ESM2G
	GFDL-ESM2M
NSF-DOE-NCAR	CESM1-CAM5

Table S1 : CMIP5 models used in the present study. The 34 models, for which we have SST, SLA and windstress available in their historical runs (at least over the 1861-2005 historical period, except CanCM4 starting in 1961).